Shelfbreak Downwelling in the Alaskan Beaufort Sea

Nicholas P. Foukal[1] [ID], **Robert S. Pickart[1]** [ID], **G. W. K. Moore[2]** [ID], and **Peigen Lin[1]** [ID]

[1]Woods Hole Oceanographic Institution, Woods Hole, MA, USA, [2]Department of Physics, University of Toronto, Toronto, Ontario, Canada

Abstract The oceanographic response and atmospheric forcing associated with downwelling along the Alaskan Beaufort Sea shelf/slope is described using mooring data collected from August 2002 to September 2004, along with meteorological time series, satellite data, and reanalysis fields. In total, 55 downwelling events are identified with peak occurrence in July and August. Downwelling is initiated by cyclonic low-pressure systems displacing the Beaufort High and driving westerly winds over the region. The shelfbreak jet responds by accelerating to the east, followed by a depression of isopycnals along the outer shelf and slope. The storms last 3.25 ± 1.80 days, at which point conditions relax toward their mean state. To determine the effect of sea ice on the oceanographic response, the storms are classified into four ice seasons: open water, partial ice, full ice, and fast ice (immobile). For a given wind strength, the largest response occurs during partial ice cover, while the most subdued response occurs in the fast ice season. Over the two-year study period, the winds were strongest during the open water season; thus, the shelfbreak jet intensified the most during this period and the cross-stream Ekman flow was largest. During downwelling, the cold water fluxed off the shelf ventilates the upper halocline of the Canada Basin. The storms approach the Beaufort Sea along three distinct pathways: a northerly route from the high Arctic, a westerly route from northern Siberia, and a southerly route from south of Bering Strait. Differences in the vertical structure of the storms are presented as well.

Plain Language Summary The weather along the Alaskan North Slope is characterized by strong storms that redistribute sea ice and water masses along and across the continental shelf. Past studies of this region have described upwelling-favorable storms, in which easterly winds transport surface waters offshore and bring water from the basin to the bottom of the shelf. In this study, high-resolution mooring data are used to provide the first comprehensive investigation of downwelling-favorable storms in this region. These storms result in westerly winds in the region that drive surface waters onshore, accelerate the shelfbreak jet to the east, and flux near-bottom shelf waters offshore into the Canada Basin. From August 2002 to September 2004, 55 downwelling storms are identified, with the most frequent occurrence in July and August. As is true for upwelling storms, ice cover strongly affects the oceanographic response to downwelling-favorable conditions. For a given wind strength, the largest response occurs during partial ice cover, while the most subdued response occurs when the ice is highly concentrated and immobile. The storms approach the Beaufort Sea along three distinct pathways: a northerly route from the high Arctic, a westerly route from northern Siberia, and a southerly route from south of Bering Strait.

1. Introduction

The transport of Pacific water through Bering Strait supplies heat, freshwater, and nutrients to the western Arctic Ocean. These relatively fresh Pacific waters ventilate the upper halocline of the Canada Basin and act as a barrier between the sea ice at the surface and the warm and salty Atlantic waters at depth. Concurrent increases in the rate of Pacific water inflow through Bering Strait (now approximately 1 Sverdrup, 1 Sv = 10^6 m^3/s; Woodgate, 2018), sea ice decline in the Canada Basin (Perovich, 2011), and freshwater content of the Beaufort Gyre (Proshutinsky et al., 2015) have led to renewed attention regarding the fate of the Pacific-origin water and the extent to which it is contributing to these changes in sea ice and freshwater.

The Pacific water flowing through Bering Strait crosses the Chukchi shelf via a set of well-documented pathways (Figure 1). Recent studies have demonstrated that there is communication between these pathways and that some portion of the water from the three main routes—through Herald Canyon, through Central Channel, and along the coast of Alaska—eventually enters Barrow Canyon. Upon exiting the canyon, a portion of the Pacific water turns eastward and forms the Beaufort shelfbreak jet
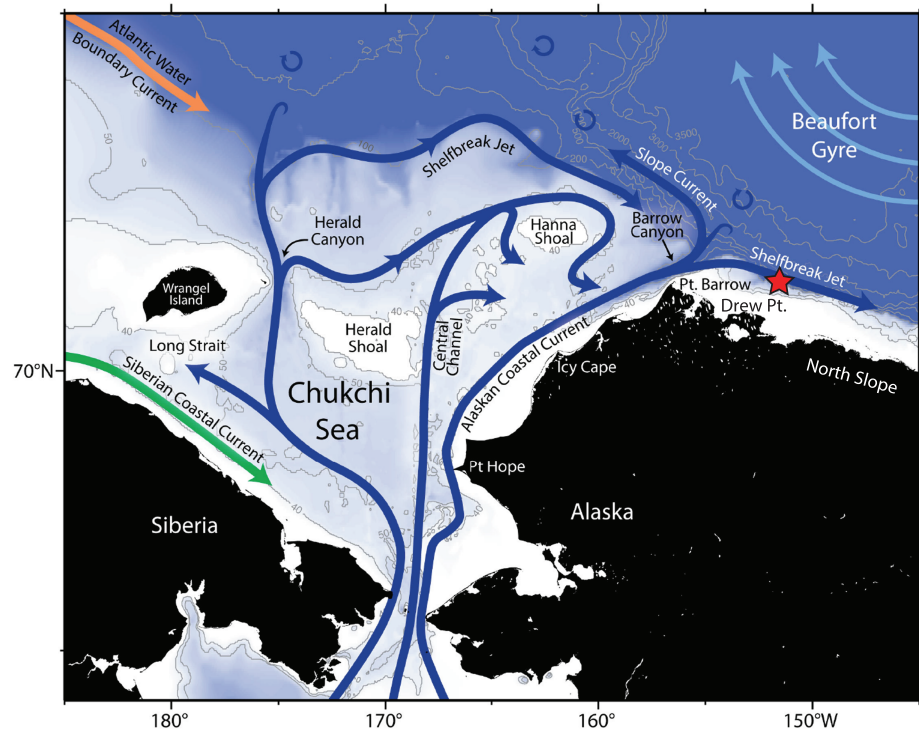
Figure 1. Schematic circulation in the Chukchi and Alaskan Beaufort Seas updated from Corlett and Pickart (2017). The location of the SBI array at 152°W is denoted with a red star. The bathymetry is colored, from ETOPO2.

(Nikolopoulos et al., 2009), while the bulk of the outflow is believed to turn westward and form the Chukchi Slope Current (Corlett & Pickart, 2017; Li et al., 2019; Spall et al., 2018). The remaining Pacific water exits the Chukchi shelf through Long Strait into the East Siberian Sea (Woodgate & Aagaard, 2005) and through Herald Canyon, which feeds the Chukchi shelfbreak jet (Pickart et al., 2010; Linders et al., 2017; see Figure 1). Using a combination of historical mooring data and shipboard data, Corlett and Pickart (2017) achieve a mass balance between the inflow through Bering Strait and the combined outflow through Barrow Canyon, Herald Canyon, and Long Strait. It has been argued, however, that some portion of the Pacific water also leaves the Chukchi Sea via subduction across the length of the shelfbreak (Timmermans et al., 2017) and via eddy formation at the mouths of the two canyons (Linders et al., 2017; Pickart & Stossmeister, 2008).

In order to reach the interior Beaufort Sea and Canada Basin, the Pacific water needs to be subsequently transferred seaward from the boundary currents that stem from the shelf. In the case of the Chukchi Slope Current, it is unclear how this happens. Corlett and Pickart (2017) determine that the current is baroclinically unstable, which could lead to an offshore flux of water. A recent study of Lagrangian float trajectories showed that, at times, a portion of the current can get entrained into the Beaufort Gyre west of the Northwind Ridge (near 160°W; S. Boury, personal communication, July, 2019). In the case of the Chukchi shelfbreak jet, it has been documented that eddies are spawned from the current (Pickart et al., 2005), likely due to baroclinic instability (Spall et al., 2008). It is uncertain if these eddies subsequently interact with the Chukchi Slope Current or if they are able to progress into the basin during time periods when the slope current is weak or absent (Li et al., 2019). In any event, Pacific water eddies are commonly observed in the southern Canada Basin (Fine et al., 2018; Manley & Hunkins, 1985; Mathis et al., 2007; Zhao & Timmermans, 2015). It also seems likely that much or most of the Chukchi shelfbreak jet is entrained into the Chukchi Slope Current at the mouth of Barrow Canyon.

It is well established that Pacific water is fluxed offshore from the Beaufort shelfbreak jet via internal forcing and external forcing. With regard to the former, mooring observations (von Appen & Pickart, 2011) and models (Watanabe, 2011) indicate that the different seasonal configurations of the current are baroclinically unstable. This is consistent with the model results of Spall et al. (2008) in which a large amount of Pacific
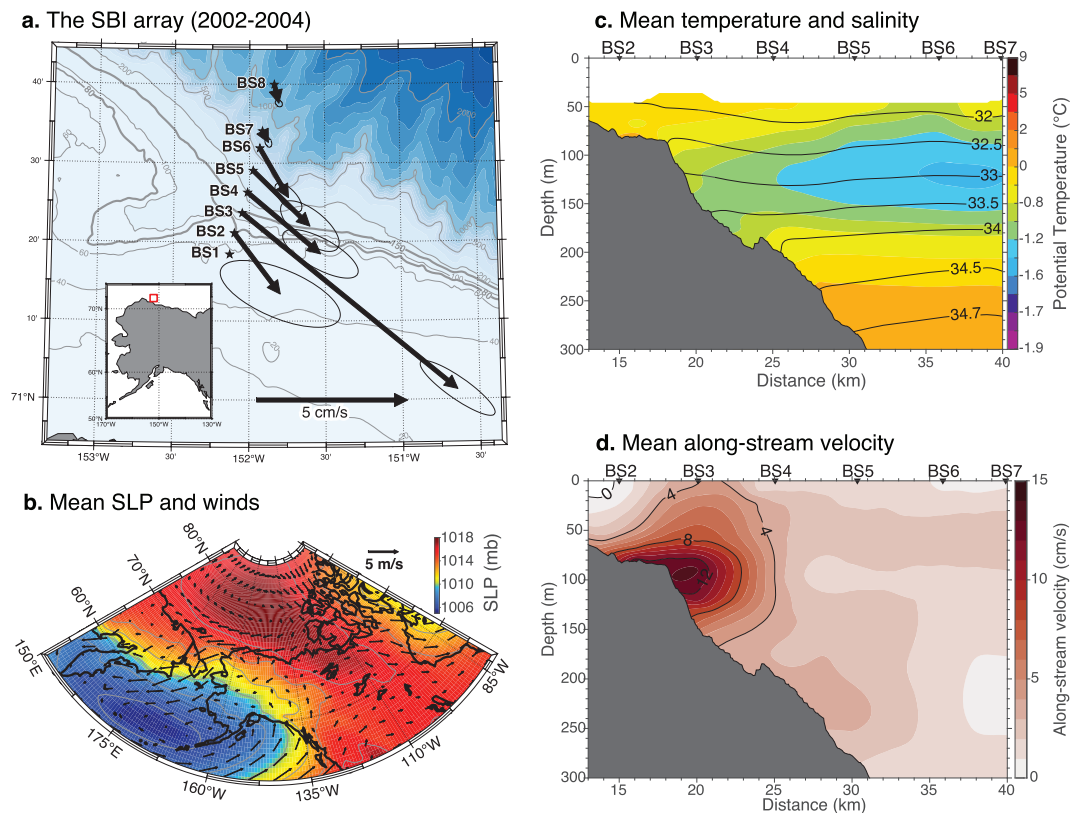
Figure 2. Two-year mean conditions at the SBI mooring array. (a) Depth-averaged velocity vectors with standard error ellipses. The bathymetry is from IBCAO v3 (color and contours). The isobaths that intersect BS2 (depth ~80 m) and BS3 (depth ~150 m) are highlighted to outline the canyon located to the west of the mooring array. The inset panel shows the study region (red). (b) Sea level pressure (color) and 10-m winds (vectors) from ERA-Interim. (c) Vertical section of mean temperature (color) overlain by salinity (contours). The mooring names are indicated along the top. (d) Vertical section of mean along-stream velocity (positive is to the southeast).

water is fluxed offshore via eddies originating from the current. Such eddies are frequently observed seaward of the current (Pickart et al., 2005). With regard to external forcing, both wind-driven upwelling and downwelling occurs along the Beaufort shelfbreak/slope. The former has been studied extensively over the past decade, using a combination of observations and models.

Much of the observational work addressing upwelling uses data from a high-resolution mooring array that was deployed roughly 150 km to the east of Barrow Canyon in the Alaskan Beaufort Sea (Figures 1 and 2a), as part of the Western Arctic Shelf-Basin Interactions (SBI) program. Analyses of these data have revealed that upwelling occurs most frequently in the winter months and under ice conditions that range from open water to 100% concentration (Schulze & Pickart, 2012). The upwelling is driven by a combination of two atmospheric centers of action, the Aleutian Low and Beaufort High (Pickart et al., 2009). A typical sequence of events is that an Aleutian low-pressure system intensifies in the Gulf of Alaska or southern Bering Sea, and the sea level pressure (SLP) gradient between this and the Beaufort High results in strong easterly winds along the Beaufort shelf and slope. The winds reverse the shelfbreak jet (so that it flows westward toward Barrow Canyon), and less than a day later upwelling commences (Pickart et al., 2009). At times, water from as deep as the Atlantic layer on the continental slope is upwelled to the Beaufort shelf. Lin et al. (2019) demonstrate that this condition tends to occur outside of the summer months when the local wind stress curl over the Beaufort slope raises the Atlantic water/Pacific water interface. At the conclusion of an upwelling event the eastward flowing shelfbreak jet is reestablished, and a deeper "rebound jet" is energized on the upper slope that accelerates the flow of Atlantic water to the east (Pickart et al., 2011). Similar upwelling events have been shown to occur along the Canadian Beaufort Sea slope (Dmitrenko et al., 2016, 2018; Kirillov et al., 2016).

The shelf-basin fluxes of heat, salt, and nutrients can be substantial during upwelling. Pickart, Spall, and Mathis (2013) analyzed a particularly energetic event in November 2003 in which the secondary Ekman circulation cell was on the order of 1–2 Sv during the peak of the event. This resulted in a transfer of heat into the basin nearly equivalent to the yearly supply of heat to the Beaufort shelf from Bering Strait and an offshore flux of freshwater equal to the year-to-year variation in freshwater content of the Beaufort Gyre. The onshore flux of nitrate from the storm was a substantial fraction of the amount utilized during primary production on the Beaufort shelf in a given year. The occurrence of upwelling along the Beaufort slope seems to be increasing as of late. Using a wind proxy for upwelling applied to the long-term Barrow meteorological time series, Pickart, Schulze, et al. (2013) showed that both the number of events and the wind strength during the events has increased in recent decades.

While upwelling drives Pacific water offshore in the upper layer via the Ekman secondary circulation, downwelling transports Pacific water offshore at depth via an oppositely sensed Ekman cell. However, in contrast to upwelling in the Beaufort Sea, there has been very little investigation of downwelling in this region. Along the Canadian Beaufort shelf/slope, Dmitrenko et al. (2016) analyzed data from three moorings near the entrance to Amundsen Gulf (~130°W) in 2003–2005. They showed that two different low-pressure systems passing north of their mooring array in January 2005 resulted in storm surges of more than a meter at a coastal tide gauge and an intensification of the eastward flow on the upper slope. Kirillov et al. (2016) used historical hydrographic data over the region to determine the atmospheric conditions that drove typical upwelling and downwelling responses. Over a 2-year study period, Dmitrenko et al. (2018) identified five downwelling events (along with a number of upwelling events). However, no study to date has described the cross-stream structure of downwelling events, nor has any documented their seasonality and dependence on ice cover.

While there is a dearth of information regarding the downwelling process in the Beaufort Sea, numerous studies have investigated the effects of the downwelling storms on the terrestrial environment along the Alaskan North Slope. The downwelling-favorable westerly winds erode the coastline because they drive Ekman transport onshore, which introduces high wave energy to the permafrost-dominated coastlines. In previous years the coast was shielded by sea ice, but, due to the earlier melt-back and later freeze-up (Frey et al., 2015), this is often no longer the case. Strikingly, rates of coastal erosion at Drew Point, the point of land closest to the SBI mooring array, have accelerated from roughly 7 m/year from 1955 to 1979 to more than 17 m/year from 2007 to 2017 (Jones et al., 2009, 2018). These rates are the fastest of anywhere in the Arctic (Barnhart, Overeem et al., 2014) in part because of the longer seasonal duration of open water. The erosion is highly episodic, with 40% occurring during less than 5% of the ice-free season (Barnhart, Anderson, et al., 2014), and rates exceeding 1 m/day over a 4-day stretch in July 2017 (Cunliffe et al., 2018), indicating that storms have a disproportionately large effect.

In this study, we use data from the high-resolution SBI mooring array in the Alaskan Beaufort Sea to describe the oceanographic conditions during downwelling. Additionally, we characterize the atmospheric forcing that drives the downwelling and show how the water column response is impacted by ice cover. The paper is structured as follows. In section 2 we describe the mooring array data along with the atmospheric reanalysis and sea-ice data used in the study. The method of identifying the downwelling storms is also explained. Section 3 addresses the kinematic and hydrographic evolution of the water column during downwelling in different ice seasons, as well as the effect of downwelling on the offshore transport of Pacific-origin water. In section 4 we assess the atmospheric forcing, including investigation of the downwelling storm tracks. Our conclusions are presented in section 5.

2. Data and Methods

2.1. The SBI Mooring Array

Eight moorings were deployed across the Beaufort Sea shelfbreak/slope from August 2002 to September 2004 at 152°W, as part of the SBI program. This location is roughly 150 km to the east of Barrow Canyon (Figures 1 and 2a). Here we use moorings BS2–BS6, which extend from the outer shelf to the 600-m isobath on the continental slope (the outer two moorings, BS7 and BS8, did not measure as frequently). The hydrography of the water column was measured using moored conductivity-temperature-depth (CTD) profilers (Fratantoni et al., 2006). These are motorized instruments that provided temperature and salinity profiles every

6 hours at 2-m vertical resolution, from 40-m depth to the bottom (the top floats of the moorings were situated at 40 m to avoid damage from ice keels). The processing procedure and accuracy of the hydrographic measurements are presented in Spall et al. (2008). Velocity was measured using upward facing acoustic Doppler current profilers (ADCPs) at the base of the moorings, providing hourly vertical profiles at 5- to 10-m resolution, extending from the depth of the instrument to within 6–31 m of the surface (progressing onshore to offshore). The reader is referred to Nikolopoulos et al. (2009) for a detailed description of the velocity data processing and accuracy. The moorings used in the study were spaced ~5 km apart, with mooring BS3 situated just seaward of the shelfbreak in 147 m of water within the core of the shelfbreak jet. Following Nikolopoulos et al. (2009), we rotate the velocities into along-stream (positive flow directed to the southeast along 125°T) and cross-stream (positive flow directed offshore along 35°T). This choice was dictated by the depth-averaged flow vectors.

2.2. Atmospheric Conditions

We use the 10-m winds from the Barrow meteorological station, obtained from the NOAA National Climate Data Center (www.ncdc.noaa.gov). The data are quality controlled, interpolated to 1-hour temporal resolution, and rotated into along-coast and cross-coast components. The winds at Barrow are highly correlated ($r = 0.92$) with the local winds at the study site derived from weather forecast products (Nikolopoulos et al., 2009), and the Barrow time series have been used extensively in previous upwelling studies (Lin et al., 2019; Pickart et al., 2011; Pickart, Schulze, et al., 2013; Pickart, Spall, & Mathis, 2013; Schulze & Pickart, 2012).

To provide a larger-scale context of the atmospheric conditions, we use ERA-Interim (ERA-I; Dee et al., 2011) SLP, 10 m winds, 500 mb height, and 500 mb winds for the region 150°E–80°W, 50°N–85°N. Vertical wind shear between the surface and 500 mb was calculated to assess the baroclinicity of the downwelling storms. ERA-I produces reanalysis fields at 0.75° resolution and 6-hourly intervals from 1979 to 2015. All 37 years were used to construct the climatology and anomalies from the climatology, as well as the storm tracks. The 2-year period 2002–2004 was extracted to determine the atmospheric forcing during the period of the mooring deployment.

2.3. Identification of Downwelling Events

We define three conditions that characterize a downwelling event at the mooring array: (1) westerly wind at Barrow (i.e., positive along-coast wind); (2) an intensification of the eastward flow of the shelfbreak jet; and (3) an anomalously light density at the base of mooring BS3 (100–132 m) in the center of the shelfbreak jet. These conditions are largely mirror images of those defined to identify upwelling events (Lin et al., 2019; Pickart et al., 2009; Schulze & Pickart, 2012) but differ slightly due to the long-term mean conditions at the mooring site. The mean winds along the southern Beaufort Sea are upwelling-favorable easterly winds (Figure 2b); thus, westerly winds are anomalous regardless of their strength. Schulze and Pickart (2012) demonstrate that easterly winds in excess of 4 m/s are required to drive upwelling at this site, but any westerly wind may cause a downwelling signature relative to the background upwelling-favorable state. Similarly, the 2-year mean shelfbreak jet is eastward (Figure 2a), and the depth-averaged velocity in the core of the current (at mooring BS3) is 9 cm/s. We consider values greater than this to represent an intensification of the current. Finally, to remove the seasonal cycle in the density signal at the base of BS3, a 45-day running mean is subtracted from the time series prior to isolating the downwelling events.

For each event, we use the initiation of the westerly winds as the start date/time and the relaxation of the density anomaly toward its state prior to the storm as the end date/time. Ideally, this would be done with an automated algorithm, but a number of issues make this impossible. Primarily, the density anomaly did not always relax completely before the next storm began. This is further complicated by the fact that there is an 8-hr lag between the wind forcing and the acceleration of the shelfbreak jet and an additional 4-hr lag before the downwelling commences. Therefore, the oceanographic response occasionally overlapped with the atmospheric forcing of the next storm. We sought to separate storms when the atmospheric forcing was clearly distinct, so determining the start and end dates for consecutive storms was an iterative process of analyzing the mooring data and the atmospheric reanalysis fields. For these reasons, together with the inherent variability in the mooring time series, visual inspection was necessary to robustly define the downwelling events.

2.4. Storm-Dependent Rotation Angles

Our analysis reveals that during downwelling events, the enhanced shelfbreak jet was not always oriented in the same direction (recall that the mean orientation of the jet over the 2-year record is 125°T). Schulze and Pickart (2012) find the same to be true regarding the orientation of the reversed shelfbreak jet during upwelling. As such, they define a storm-dependent coordinate system where the along-stream angle varies from event to event. This is necessary in order for them to detect a clear signal of an Ekman cell in the cross-stream data at BS2 (i.e., on the outer shelf). Here we follow a similar procedure and define the along-stream axis for each downwelling event as the direction of the depth-mean velocity at BS3 averaged over the middle half (25–75%) of the storm's duration (the rotation angles are not sensitive to the specific definition).

2.5. Definition of Ice Seasons

To investigate the influence of sea ice on downwelling, we use ice concentration data as well as ice velocity data. Ice concentrations from the Advanced Microwave Scanning Radiometer-Earth Observing System (AMSR-E; Spreen et al., 2008) satellite are spatially-averaged over the region surrounding the array to construct a single time series. The ice speed time series is derived from the top-most bin of an upward facing ADCP at mooring BS2 on the outer shelf (we do not have ice velocity data at the other mooring locations). The reader is referred to Pickart et al. (2009), Schulze and Pickart (2012), and Lin et al. (2016) for details on the construction of these two time series. Using this information, we define four ice seasons: open water, partial ice, full ice, and fast ice. Open water season is the period when the ice concentration is less than 10%, while partial ice season is the period when the ice concentration is between 10% and 70%. Full and fast ice seasons both occur when the ice concentration is greater than 70%. Previous work has shown that ice can still be mobile even if the concentration is near 100% (Pickart et al., 2009). Thus, we differentiate between full ice (mobile) and fast ice (immobile) by defining a threshold of 4 cm/s in the ice speed record. When the ice speed is less than 4 cm/s, it is evident that the ice is moving slowly enough to strongly inhibit the transfer of energy from the atmosphere to the ocean. This threshold for ice speed thus represents the transition from when the ice was clearly mobile to when it was completely or mostly fast.

3. Downwelling Conditions From the In Situ Data

3.1. Characterization of Downwelling Events

Over the 25-month mooring deployment, a total of 55 downwelling events were identified. These are marked in Figure 3 in relation to the along-coast wind, the depth-averaged velocity of the shelfbreak jet, and the near-bottom density anomaly in the vicinity of the shelfbreak. Recall that the downwelling events correspond to westerly winds, enhanced eastward flow of the shelfbreak jet, and anomalously light bottom water residing near the shelfbreak. One sees that the events are often clustered (an extreme example of this is July 2003, when downwelling occurred for 76% the entire month) but can be spaced out as well. Overall, downwelling conditions occurred during 27% of the mooring record. Interestingly, upwelling occurred 23% of the time (Schulze & Pickart, 2012), meaning that the Beaufort shelfbreak jet was wind-forced half of the time during the SBI time period.

Downwelling occurred during all ice seasons (Figure 4). There were 19 events during open water, 12 events during partial ice cover, 17 events when the ice cover was full but mobile, and 7 events in fast ice conditions (full ice cover, immobile). This corresponds to the following percentages of each ice season covered by downwelling: 34% of the open water season, 43% of the partial ice season, 23% of the full ice season, and 18% of the fast ice season. Partial ice stands out as a time when considerable downwelling occurs, as 22% of the events (12/55) occurred during just 14% of the 2-year time period. The opposite extreme was fast ice, where 13% of the events (7/55) occurred during 26% of the 2-year time period.

Over all 55 downwelling events, the mean shelfbreak jet is accelerated in nearly the same direction (127.7°T) as the long-term mean flow (125°T), with little deviation between events (Figure 5) and no difference between the ice seasons. Three storm events stand out as outliers: two with flow angles near 90°T and one near 155°T. Analysis of the storm tracks (section 4.1) reveals that these storms were anomalous; the two zonally oriented shelfbreak jet storms occurred sequentially at the beginning of our record in August 2002 and stalled offshore of the study site for over 5 and 7 days, respectively. The stalling of the storms caused the average winds, and resultant velocities at the shelfbreak, to be oriented more zonally than along shore
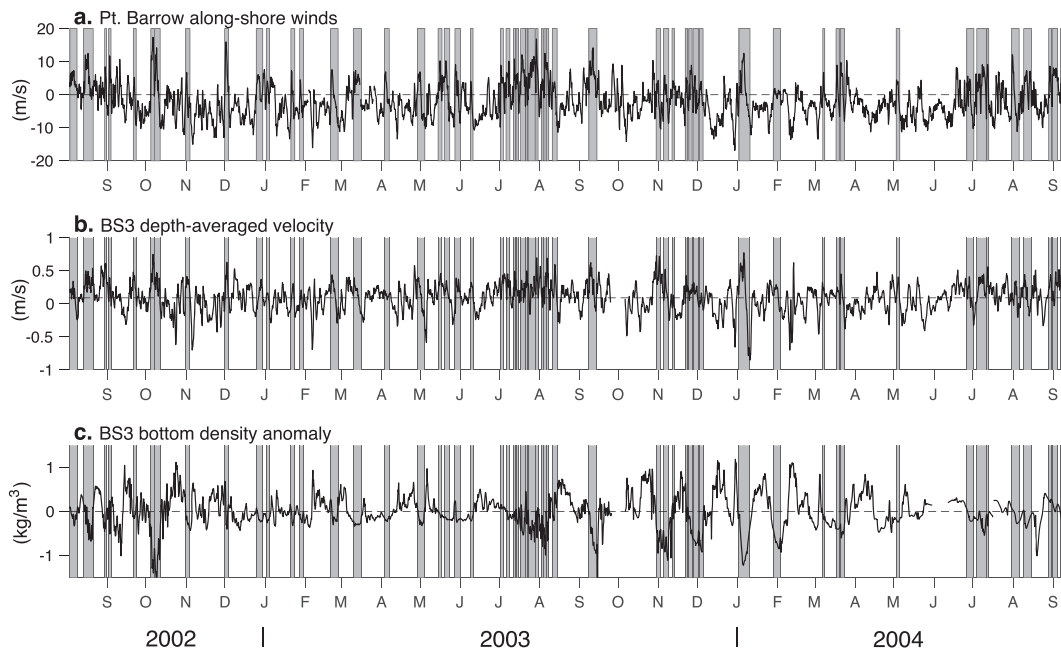
Figure 3. Downwelling events during the 2-year mooring deployment, indicated by the gray vertical bars, in relation to (a) the along-coast wind at Barrow (positive is westerly); (b) the depth-averaged along-stream velocity at mooring BS3, where the time-mean value is indicated (black dashed line); and (c) the near-bottom density anomaly at mooring BS3.
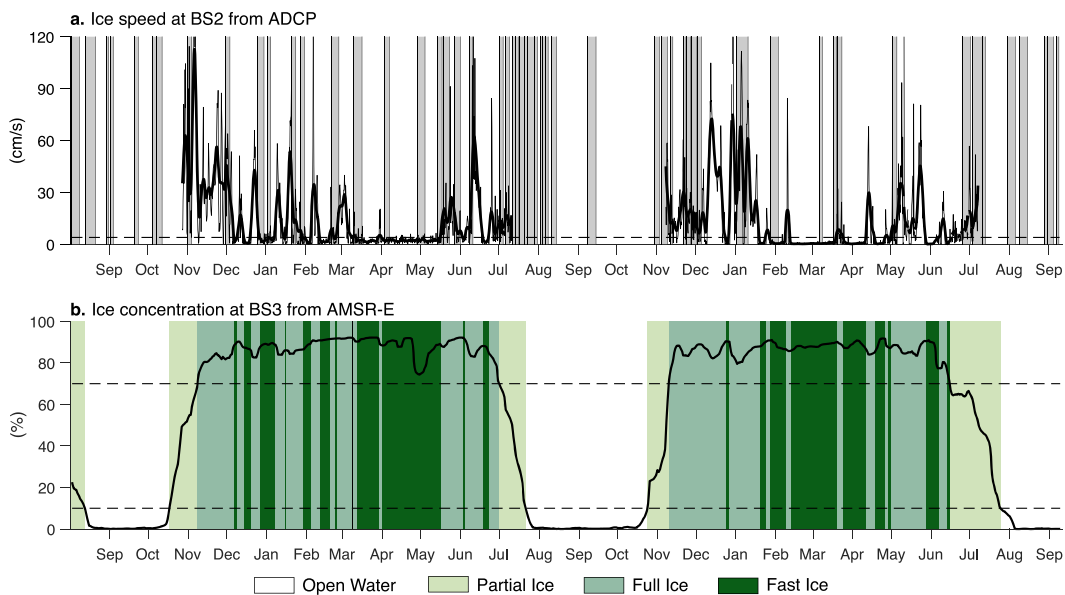

Figure 4. Ice time series used to define the four ice seasons. (a) Ice speed at mooring BS2 at hourly resolution (light gray line) and smoothed with a 5-day running mean (thick black line). The gray vertical bars denote the 55 downwelling events, and the black dashed line is the 4-cm/s threshold used to delineate between the full mobile ice and fast ice conditions. Ice speeds are shown for periods when the ice concentration exceeded 50%. (b) Ice concentration at the SBI array site. The different ice conditions are color coded (see the legend). The black dashed lines show the 10% and 70% ice concentration thresholds used to delineate the partial ice season.
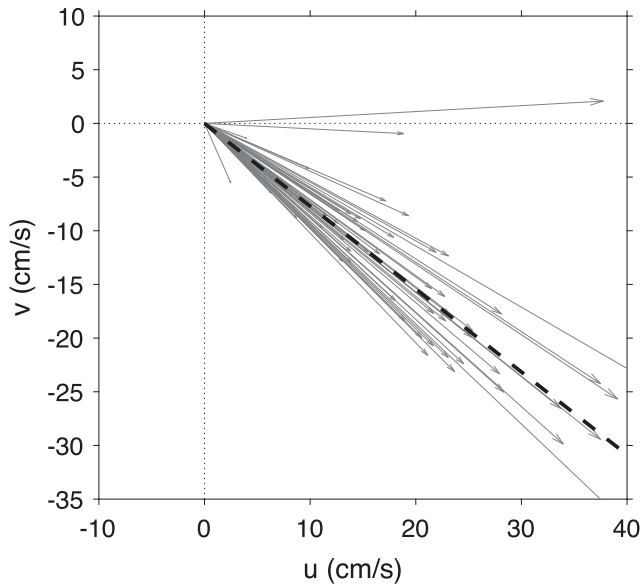
Figure 5. The depth-averaged flow vector at mooring BS3 for each downwelling event. Thick black dashed line denotes the average flow direction (127.7°T).

(i.e., northwesterly). The other outlier storm originated in the central Beaufort Sea and arrived at the study area directly from the northeast, causing the shelfbreak jet to veer toward the coast, albeit weakly.

To characterize the strength of the storms, we compute the cumulative Ekman transport (Huyer et al., 1979) as has been done for upwelling storms (e.g. Lin et al., 2019):

$$Cumulative\ Ekman\ transport = \frac{1}{\rho_0 f} \int_{t_{start}}^{t_{end} - t_{lag}} \tau(t)\ \mathrm{d}t$$

where ρ_0 is a reference density (1,025 kg/m³), f is the Coriolis parameter (1.4×10^{-4} 1/s), t_{start} and t_{end} are the start and end dates for the downwelling event, t_{lag} is the storm-dependent lag between the wind and the density anomaly, and $\tau(t)$ is the along-coast wind stress (N/m²). Cumulative Ekman transport takes into account both storm strength and duration for a given downwelling event. The end point of integration is shifted earlier to account for the restoration of easterly upwelling-favorable winds prior to the end of the event, which is explained further in section 3.2. The cumulative Ekman transport was weakest during the fast ice season, while the other three seasons were statistically indistinguishable from each other.

To compare the strength of the oceanographic response to the cumulative Ekman transport, Lin et al. (2019) define an upwelling index as the time integral of the bottom density anomaly near the shelfbreak. They find a clear relationship between this index and the cumulative Ekman transport, in that stronger storms result in stronger upwelling. We find the analogous result for downwelling. This is quantified in Figure 6a, where we display both the downwelling events and the upwelling events from Lin et al. (2019). The linear fit is similar for both cases (indistinguishable within the 95% confidence limits). In general, it is apparent that upwelling events have stronger cumulative Ekman transport than have downwelling events. This is because the background winds are easterly (upwelling favorable), so comparable anomalies from the mean wind result in larger cumulative Ekman transports for upwelling.

Are there differences in the downwelling response due to ice cover? The strongest response occurred during partial ice cover (Figure 6b, yellow), while a weaker response occurred for open water and full ice (comparable to each other; not shown). A similar result was found for upwelling (Schulze & Pickart, 2012). The explanation is that when there is partial ice cover, the sparsely distributed, mobile ice keels—with limited or no internal ice stress—lead to stronger surface stress for a given wind strength. This is supported
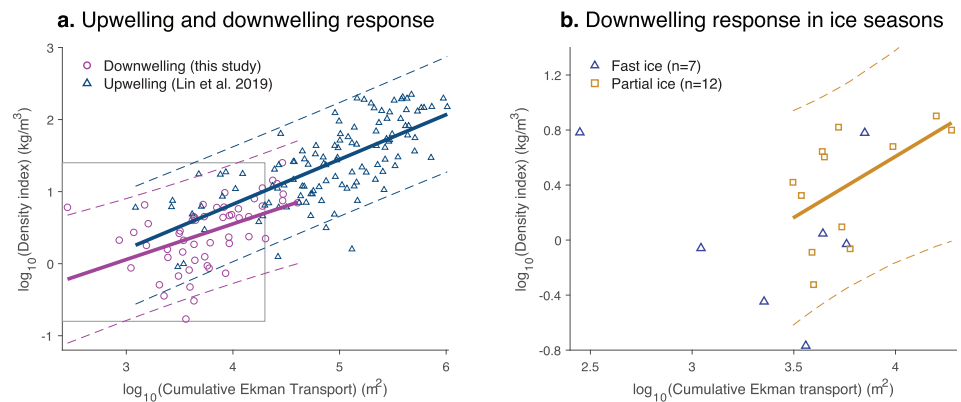

Figure 6. Sensitivity of the cumulative near-bottom density response to the cumulative wind forcing (see text). (a) Comparison of downwelling response (this study) to upwelling response (Lin et al., 2019). Thick solid lines are the least squares linear regression, dashed lines are the 95% confidence intervals of the linear fit, and the gray box outlines the region shown in panel b. (b) The downwelling cases of partial ice and fast ice (see the legend). There is no statistical trend for the fast ice events.

by theory, models, and observations (Pite et al., 2002; Williams et al., 2006; Pickart, Spall, & Mathis, 2013; Martin et al., 2014). The only ice season that displays no relationship between storm strength and downwelling strength is the fast ice season (Figure 6b, blue), which is to be expected since, locally, the wind stress is not communicated to the ocean.

3.2. Downwelling Composites

To further evaluate the downwelling responses in varying ice seasons, we construct composite downwelling events for each of the ice seasons (Figures 7–10). We interpolate the various fields onto 100 evenly spaced time intervals, with time = 0 corresponding to the initiation of the westerly winds in the Barrow record and time = 1 corresponding to the relaxation of the isopycnals at the end of the event. During this process, the storm durations are normalized to facilitate comparisons between storms. The mean duration was 3.25 ± 1.80 days, and we discuss the variability in section 4.2. The events are then collated by ice season and averaged together. For each composite, "peak downwelling" is defined as the period when the bottom density anomaly is at or near its minimum value (gray shading in panels a and b of Figures 7–10). The temperature, salinity, isopycnal displacement, and along-stream velocity are then averaged over the peak downwelling period to create canonical vertical sections for each ice season (the cross-stream velocity is treated separately in section 3.3). The isopycnal displacement is calculated as the difference in the depth of the isopycnals during the peak downwelling compared to their depth during the undisturbed state (i.e., when there is no downwelling or upwelling). We also show the along-stream velocity anomaly from the undisturbed state (panel f of Figures 7–10).

The open water period (generally August through early October; Figure 4b) corresponds to the time when the shelfbreak jet is typically surface-intensified and advects warm Pacific summer water (Schulze & Pickart, 2012; see the contours in Figure 7f). The open water downwelling composite (Figure 7) shows that the enhanced shelfbreak jet is also surface-intensified, with an anomaly close to 30 cm/s. In this state, the volume transport of the Pacific water is 0.93 Sv, compared to 0.25 Sv during the undisturbed state (i.e., in the absence of downwelling or upwelling). The along-stream velocity signature of the enhanced jet extends far offshore, with strong flow at mooring BS5 over the midcontinental slope. This is in contrast to the open water upwelling scenario, where the reversed shelfbreak jet is more narrow (Schulze & Pickart, 2012).

The downwelling composites of partial and full ice (Figures 8 and 9) are similar to one another, with bottom-intensified flow trapped to the shelfbreak (at mooring BS3, Figures 8e and 9e). In both cases, the velocity anomaly is largest at middepth, corresponding to a slight widening of the current as well (Figures 8f and 9f). These similarities are perhaps not surprising because the ice in both of these composites is mobile. However, as noted above, there is less ice and less internal ice stress in the partial ice case than in the full ice case; hence, more energy is communicated to the water column. Consequently, the partial ice composite has both larger isopycnal displacements (max >60 m) from the undisturbed state than does the full ice composite (max ~35 m), as well as stronger along-stream transport (0.57 versus 0.47 Sv).

The fast ice downwelling composite (Figure 10) stands out from the other three ice seasons primarily due to the small magnitude of the downwelling response. The strength of the density anomaly at the shelfbreak (Figure 10b; 0.16 kg/m^3) is only half of the open water composite (Figure 7b; 0.32 kg/m^3), and the enhanced shelfbreak jet transport is smallest (0.33 Sv, which is not that much larger than the undisturbed value of 0.25 Sv). The along-stream velocity anomaly is strongest at middepth, as it is for the other two ice cases, in contrast to the open water case where the anomaly is largest in the upper layer. Since we only have ice velocity information at mooring BS2 on the outer shelf, we are unable to determine if the ice was fast offshore of the shelfbreak. As noted above, the cumulative Ekman transport for the fast ice case is weaker than for the other ice seasons. In addition, the composited wind time series for fast ice (Figure 10a) has the smallest peak value (4.5 m/s). This likely factors into the generally weak downwelling response for this ice season. Schulze and Pickart (2012) argue that the upwelling response during fast ice conditions is related to along-stream variation in ice cover and nonlocal forcing. This is presumably true for downwelling as well and deserves further study.

In contrast to that for the fast ice case, the wind composite for the open water season has the strongest peak value (7.3 m/s; Figure 7a). Since the cumulative Ekman transports are comparable for open water, partial ice, and full ice, this implies that the open water storms are generally shorter (which we verified). Interestingly,
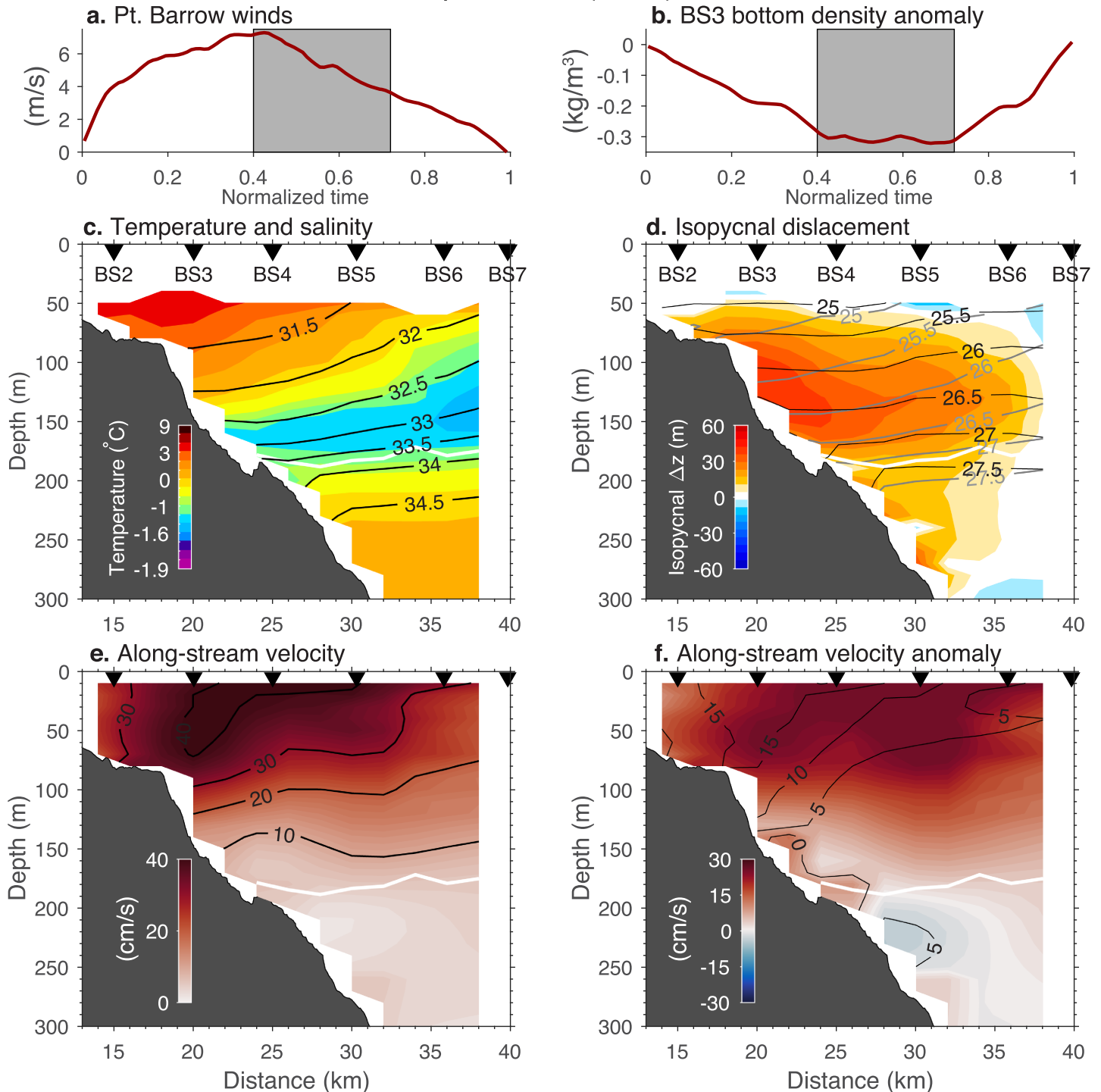
Figure 7. Composite conditions for the 19 downwelling events during open water conditions. (a) Along-coast winds at Barrow on a normalized time axis with 0 corresponding to the initiation of the event and 1 corresponding to the end of the event. Gray bars in panels a and b show the time period of peak downwelling (corresponding to normalized time 0.40–0.72), over which panels c–f are averaged. (b) Bottom density anomaly at mooring BS3 near the shelfbreak. (c) Temperature (color) and salinity (contours) during peak downwelling. The Pacific-Atlantic water boundary (white line) is shown in panels c–f. (d) Depth of the isopycnal displacement (color) during peak downwelling (gray contours) with respect to the undisturbed conditions in the open water season (black contours). (e) Along-stream velocity (colors and contours) during peak downwelling. The velocities are rotated according to the storm-dependent rotation angles shown in Figure 4 prior to compositing. (f) Anomalies of the along-stream velocity (color) relative to the undisturbed state (contours).
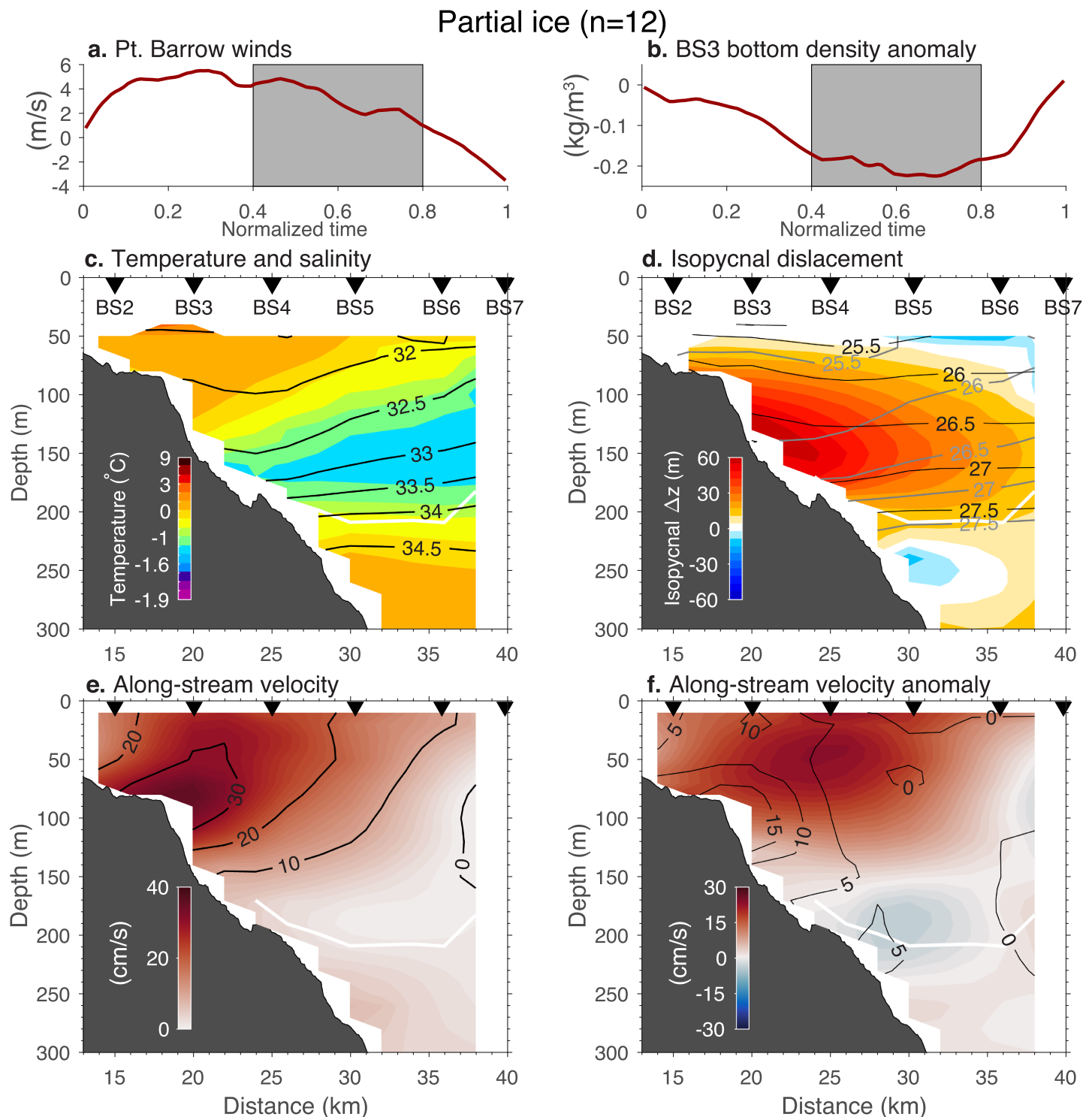
Figure 8. As in Figure 7 but for the 12 downwelling events during partial ice cover. The period of peak downwelling (shown as gray bars in panels a and b) covers normalized time steps 0.40–0.80.

the winds relax to zero at time = 1 in the open water composite, whereas for the other three ice seasons the winds become easterly by time step 0.7. In the partial ice and full ice composites, the winds approach −4 m/s by the end of the event. Schulze and Pickart (2012) show that 4 m/s easterly winds are the threshold for driving upwelling at the shelfbreak. Thus, upwelling immediately follows 58% of the downwelling events
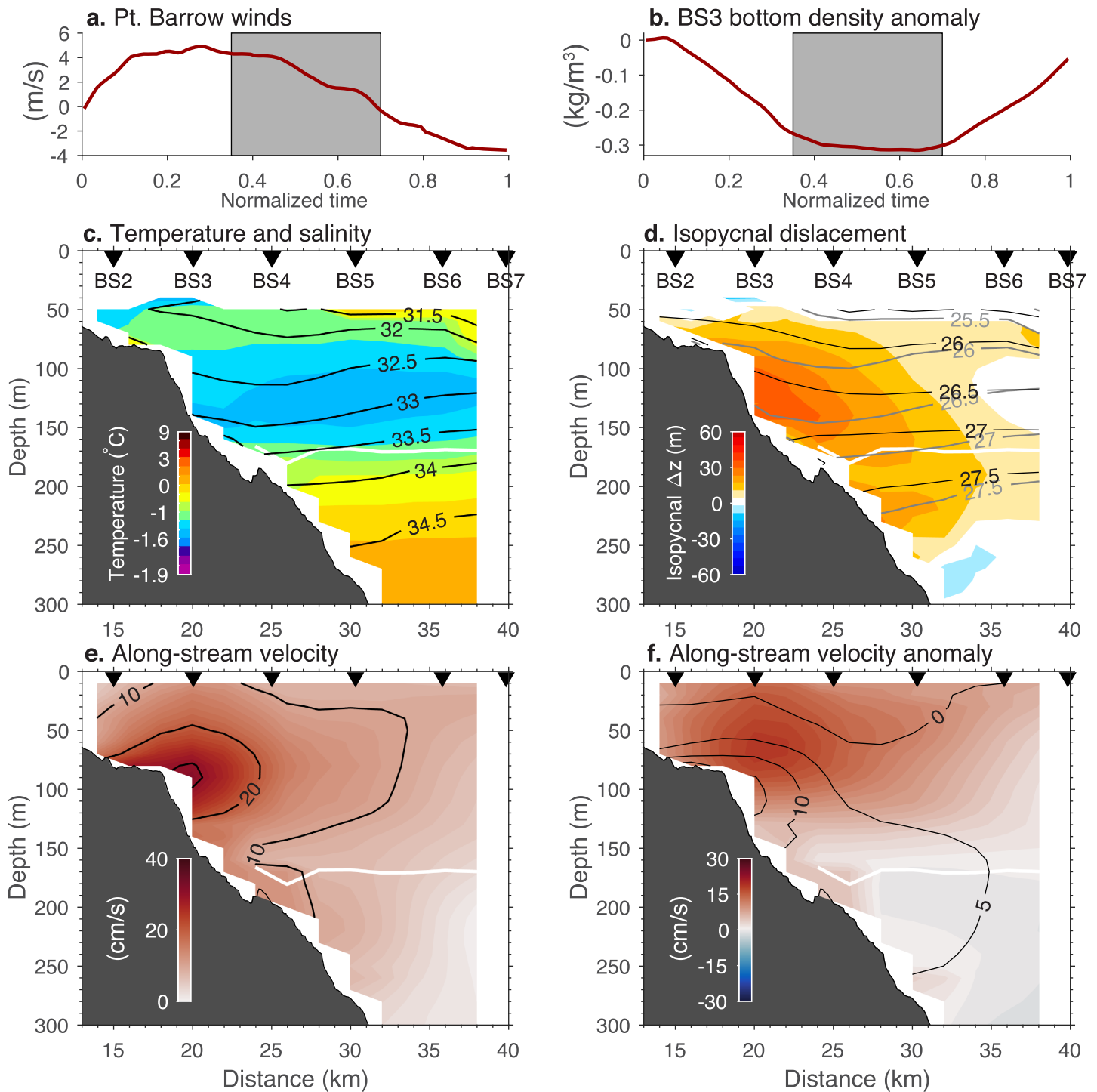
Figure 9. As in Figure 7 but for the 17 downwelling events during full ice cover. The period of peak downwelling (shown as gray bars in panels a and b) covers normalized time steps 0.35–0.70.

in partial ice and 59% of the events in full ice, compared to only 26% in open water. This can be understood climatologically in that the Aleutian Low and Beaufort High are weakest in the open water season; thus, a relaxation to mean winds in open water is closer to zero versus that in the other ice seasons.
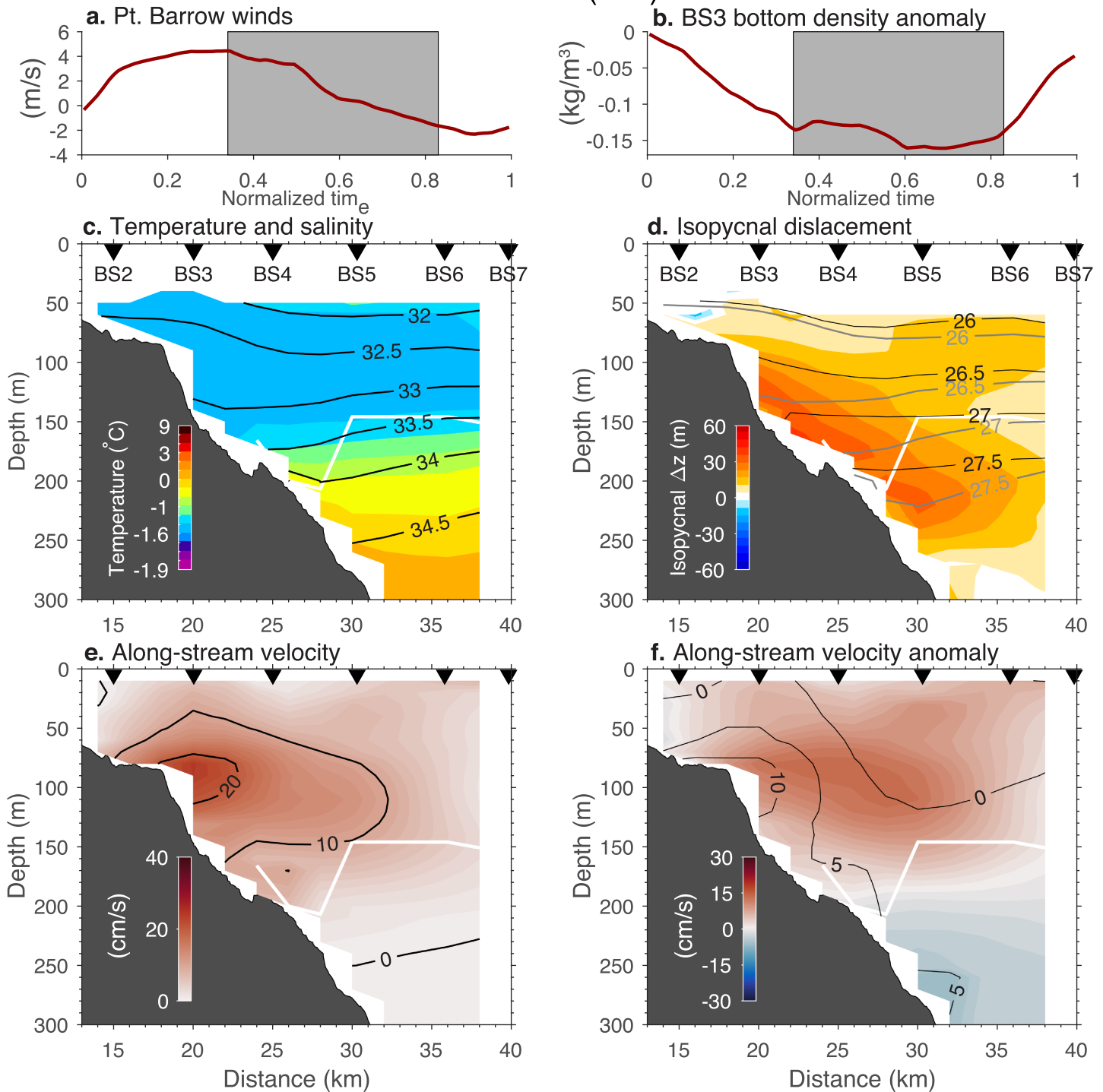
Figure 10. As in Figure 7 but for the seven downwelling events during fast ice cover. The period of peak downwelling (shown as gray bars in panels a and b) covers normalized time steps 0.34–0.83.

To further compare the ice season composites (Figures 7–10), we define the boundary between the Pacific water and the Atlantic water as the location of maximum Ertel potential vorticity (or equivalently maximum vertical stratification; see Nikolopoulos et al., 2009). This is displayed as white lines in panels c–e of Figures 7–10. In all four composites, the Pacific-Atlantic water interface corresponds to a local minimum

in the vertical isopycnal displacement because the increase in stratification at this depth results in a smaller deflection of the isopycnals. In fast ice, this interface seems to be less of an inhibitor, and the depressed isopycnals extend into the Atlantic layer, possibly reflecting nonlocal forcing. In each of the composites, the along-stream velocity decreases (or stays near zero) in the Atlantic layer, whereas during upwelling the Atlantic water is advected eastward within the rebound jet at the conclusion of the event.

The isopycnals are displaced the most in the partial ice case, followed by open water, full ice, and fast ice (although the latter two are roughly comparable). A consideration when comparing the isopycnal displacement between ice seasons is the background stratification in the undisturbed state (black contours). The background stratification is strongest in open water, weaker in partial ice, weaker still in full ice, and weakest fast ice (the 27.5 isopycnal is consistently at 200 m in all of the ice seasons, and the lightest isopycnal in open water is 25.0, compared to 25.5 in partial ice and 26.0 in full ice and fast ice). Thus, for a given forcing at the ocean's surface, we would expect the strongest isopycnal displacements for fast ice and the weakest for open water. This is the opposite of what we observe (greater displacements for open water versus fast ice), which implies that the strength of the winds and the effectiveness with which the wind stress is transmitted to the ocean plays an important role in the magnitude of the isopycnal displacement.

3.3. Cross-Shelf Fluxes

To investigate how downwelling affects the ventilation of the interior halocline, we consider the cross-stream circulation. During downwelling, onshore flow in the upper layer and offshore flow in the lower layer flux heat and freshwater across the shelfbreak. In our time series, we find that the Ekman cells are often difficult to isolate due to their weak magnitudes compared to the along-stream velocities. Thus, an error in determining the along-stream flow angle for the storm, or a time-varying angle during the storm (e.g., Pickart, Schulze, et al., 2013), leads to the along-stream velocity signal being folded into and possibly dominating the signal in the cross-stream velocity. Due to this difficulty, we identify the times during each event (from the time-normalized storm database) when there is a clear Ekman cell at the edge of the shelf as defined by onshore flow in the upper 40 m and offshore flow in the layer below this. These time steps were not required to occur sequentially, though they tended to cluster during the middle of the storms. Schulze and Pickart (2012) calculate an Ekman depth of 40–50 m at the BS2 mooring for upwelling storms (our results are not sensitive to the precise choice). The different ice seasons are treated separately, and we consider both BS2 and BS3 (i.e., the moorings on either side of the shelfbreak).

The most robust Ekman cells occur in open water conditions, with 9 (11) of the 17 storms having Ekman cells at BS2 (BS3) for over 10% of the storm's duration. In contrast, only 1 of the 12 storms in the partial ice season had an Ekman cell at BS2 for over 10% of the storm's duration. Such low percentages demonstrate the inconsistent presence of the Ekman cells, although it is clear that there are differences between these two ice seasons. Notably, shorter storms tend to have more robust Ekman cells. The probable reason for this is that a single flow angle is more representative for a shorter storm, while for longer storms the shelfbreak jet is more variable. Hence, using multiple rotation angles for the longer storms would increase our Ekman cell detection rates, as was done by Pickart et al. (2011) for an in-depth analysis of a single upwelling storm.

We found that unambiguous Ekman circulation occurs more often at BS3 than at BS2, which is in contrast to the upwelling Ekman cells detected by Schulze and Pickart (2012). We suspect that this is due to the bathymetry around the SBI array. To the west of the array, there is a canyon that extends down to the 100 m isobath, whereas to the east, the bathymetry is relatively straight (Figure 2a). When westerly winds accelerate the shelfbreak jet to the east during downwelling, the SBI array is in the wake of this canyon and the measured velocities are likely influenced by local canyon effects (e.g., eddies shed as a result of the complex bathymetry). By contrast, during upwelling, the shelfbreak jet is reversed to the west, so the canyon is downstream of the mooring array. Hence, the velocities at BS2 are likely more stable during upwelling. This effect is felt more strongly at BS2 than at BS3 because the 80 m isobath (depth of BS2 is 81 m) is deflected more strongly by the canyon than is the 150 m isobath (depth of BS3 is 147 m). Thus, the more robust cross-stream velocity signature seen at the edge of the shelf for upwelling versus downwelling is possibly due to local bathymetry rather than to inherent differences between the two processes.

For each of the downwelling storms, we average the cross-stream flow over the period that an Ekman cell is present, then composite these for the different ice seasons. The resulting profiles are shown in Figure 11 for
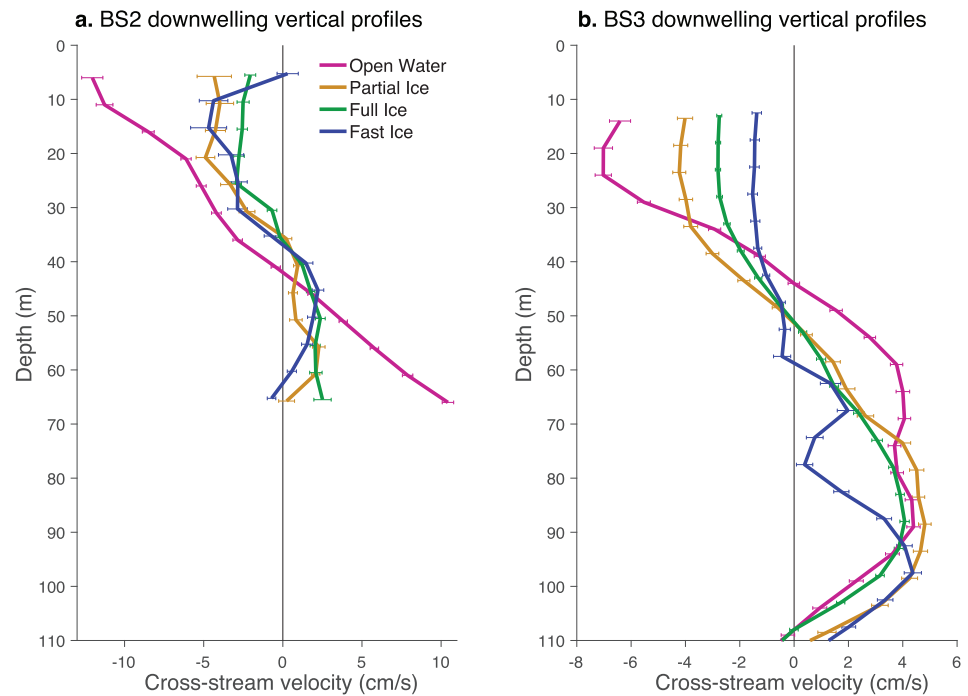
Figure 11. Cross-stream composite circulation at (a) BS2 and (b) BS3 during periods when downwelling Ekman cells are detected. Error bars depict the standard errors over the storms in each ice season.

BS2 and BS3. As noted above, the peak winds are strongest during the open water season, and, as such, the cross-stream flows are largest then. This is particularly true at the outer shelf (mooring BS2) where both the onshore and offshore flow exceed 10 cm/s. By contrast, the Ekman cells for the other ice seasons are less than 5 cm/s. For the fast ice case, the secondary circulation is zero at the uppermost bin, the implication being that it changes sign near the surface. This is consistent with an immobile ice cover where the Ekman flow is directed offshore for an eastward flowing shelfbreak jet. Schulze and Pickart (2012) found the analogous result (onshore-directed near surface flow) for the fast ice upwelling events. Seaward of the shelfbreak (mooring BS3) the Ekman cells extend to roughly 110 m (the depth of the shelfbreak is 85 m) and are generally on the order of 5 cm/s. The weakest cell occurs during the fast ice case, in line with the generally weak response in density anomaly and along-stream flow for this ice season. Below 110 m, the cross-stream flow changes sign and becomes onshore for all of the ice seasons.

It is of interest to document which water masses are fluxed offshore during the downwelling and to calculate their cross-stream volume flux. We follow previous definitions for the different types of Pacific water (e.g., Pickart et al., 2019; Pisareva et al., 2015). The two Pacific summer waters are Alaskan Coastal Water (ACW), which derives from continental run-off into the Gulf of Alaska and Bering Sea, and Bering Summer Water (BSW), which is a combination of Anadyr Water and central Bering shelf water, which mix north of Bering Strait (Coachman et al., 1975). The ACW is warmer and fresher than the BSW. From late summer to early fall the Beaufort shelfbreak jet is surface-intensified and advects primarily ACW. BSW is the predominant water mass found in the shelfbreak jet just before and after this time period (von Appen & Pickart, 2012). The two Pacific winter waters are Newly Ventilated Winter Water (NVWW) and Remnant Winter Water (RWW). The former is recently formed and is near the freezing point, while the latter is later-season winter water that has been warmed by a combination of solar heating and mixing with summer waters (Gong & Pickart, 2016). The shelfbreak jet advects both types of winter water over the remainder of the year (Brugler et al., 2014).

The water masses above the shelfbreak (50–110 m at BS3) during the initiation of downwelling span a wide range of temperatures from the warm ACW to the near-freezing NVWW (Figures 12a and 12b). The overall distribution of temperature and salinity in a "U-shape" is indicative of the three main water classes advected by the shelfbreak jet: warm and fresh Pacific-origin water, highly saline Atlantic-sourced water, and near-
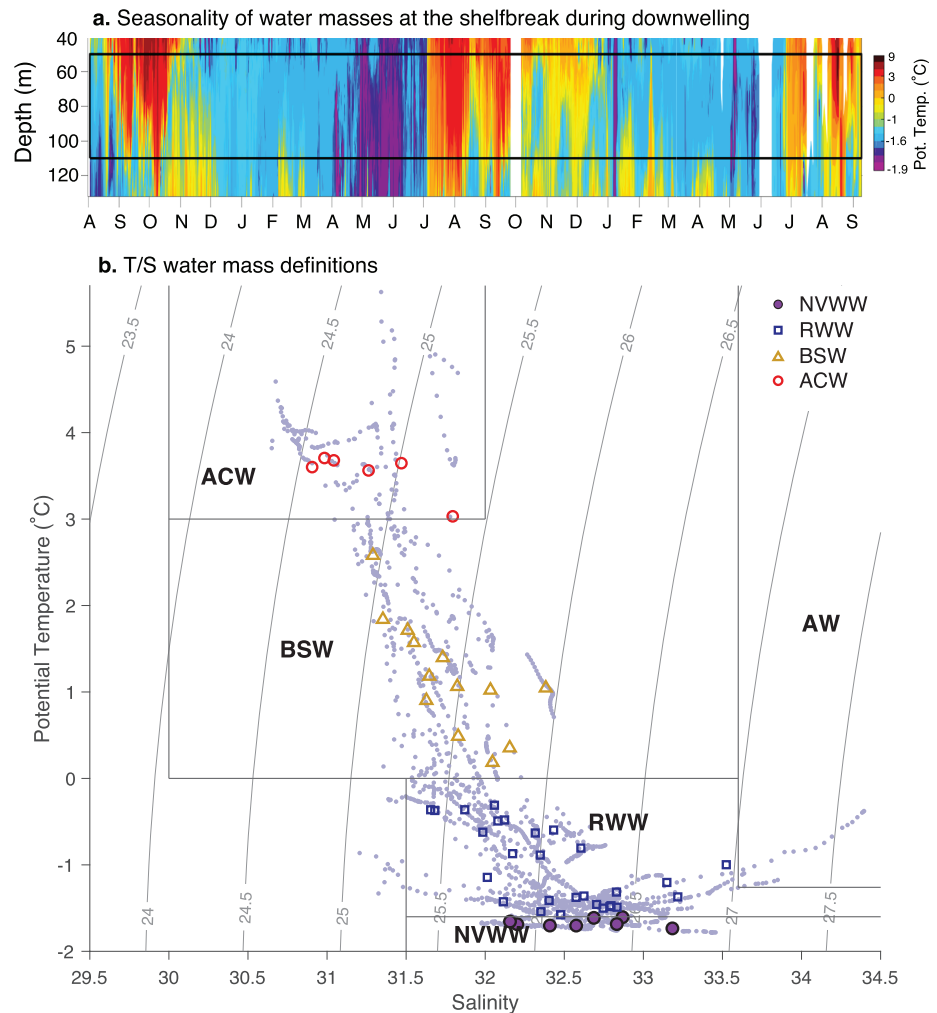
Figure 12. (a) Temperature as a function of depth and time at mooring BS3 seaward of the shelfbreak. Regions of no data are white. The black box outlines the bottom layer of the Ekman cell (50–110 m), over which the temperature and salinity in panel b and Figure 13b is plotted. (b) Water masses in the lower layer of the Ekman cell at BS3 at the initiation of each downwelling event, categorized in T-S space. The colored symbols are the T/S properties averaged over the 50- to 110-m depth range shown in panel a at the initiation of downwelling. The colored symbols match those used in Figure 13b. The light blue circles show the T/S properties at each depth to demonstrate the full range of T/S values during the initiation of downwelling. The different Pacific water masses are described in the text: ACW = Alaskan Coastal Water; BSW = Bering Summer Water; NVWW = Newly Ventilated Winter Water; RWW = Remnant Winter Water. The Atlantic Water (AW) is also marked.

freezing Pacific winter water that is ventilated locally in winter. This last water mass provides the inflection point of the U-shape.

The most common water mass fluxed offshore was RWW (28 events), followed by BSW (13 events), ACW (6 events), and NVWW (8 events). Close inspection of Figure 12b reveals a "bimodal" distribution of the RWW temperature: In roughly half the cases the water is cold and close in properties to the NVWW, while the remaining cases are closer to the warmer BSW. We note that the division between water masses used here is not precise (which has been noted in many previous papers), so we consider the coldest RWW as similar in nature to the NVWW. As such, we can conclude that 23 of the downwelling events (42% of the events) flux winter water that has been in recent contact with atmosphere into the basin. This represents an effective mechanism for moving Pacific water off the shelf into the Beaufort Gyre. Once these water masses are beyond the shelfbreak, they readily mix with the waters in the interior Canada Basin and thus ventilate the cold halocline. The key here is that the water masses cross the dynamic boundary of the shelfbreak.
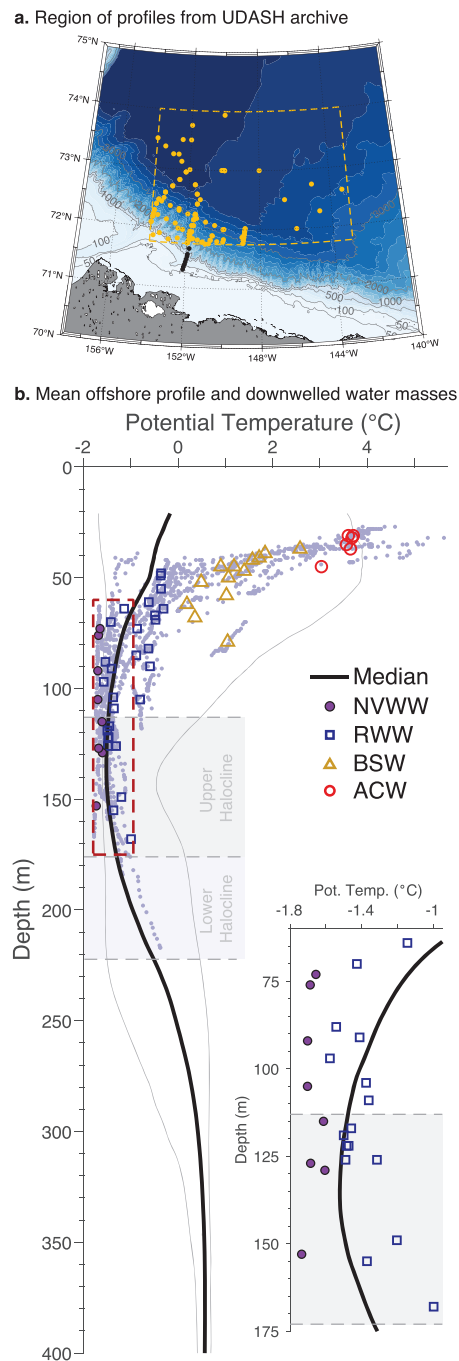
Figure 13. (a) Map of the region (71.5–74°N, 154–143°W) used to extract the data for the vertical profile displayed in panel b. The yellow dashed line outlines the selected region, and the yellow circles show the location of the 127 profiles. The bathymetry (color shading) and SBI moorings (black circles) are shown for reference. (b) Average temperature profile (thick black line) and 95% confidence intervals (thin gray lines) for the interior of the Beaufort Sea. The water masses identified in the lower layer of the Ekman cell (50–110 m) at BS3 are plotted at the depth of their density horizon in the vertical profile. The upper halocline is marked with the gray box bounded by dashed lines. The inset is an enlarged view of the region outlined by the red dashed box. The Pacific water masses are as follows: ACW = Alaskan Coastal Water; BSW = Bering Summer Water; NVWW = Newly Ventilated Winter Water; RWW = Remnant Winter Water.

To investigate which part of the Beaufort Sea halocline is ventilated during the different downwelling events, we construct an average vertical profile of the interior Beaufort Sea using all available hydrographic data offshore of the mooring array collected during 2002–2004 (Figure 13). This is done by extracting temperature and salinity data from the Unified Database of Arctic and Subarctic Hydrography (UDASH) archive (Behrendt et al., 2018), which includes summer data from ships as well as winter data from ice-tethered profilers (Krishfield et al., 2008; Toole et al., 2011). In total, there are 127 profiles in the offshore box (Figure 13a) from 2002 to 2004. The median and 95% confidence interval of these 127 profiles are shown in Figure 13b. We exclude the top 20 m of the water column from the figure because of the large seasonal differences there and the relatively sparse amount of winter data, which together result in an unrepresentative view near the surface.

The interior profile is characterized by warm water, composed of a mixture of ACW and BSW, above the layer of cold Pacific winter water (see also Steele et al., 2004; Zhao & Timmermans, 2015). Following Pickart (2004), we use the vertical gradient of the mean salinity profile to define the cold halocline, that is, the region of maximum gradient, and divide this into an upper and lower portion (separated by the peak value of the gradient). These are marked in Figure 13b by gray dashed lines. One sees that the upper halocline encompasses much of the Pacific winter water layer, including the temperature minimum (see inset panel), though the Pacific winter water layer extends well above the upper halocline.

Next we match the density of the water masses fluxed off the shelf for each event (defined in Figure 12) to that of the vertical profile from the interior of the Beaufort Sea. This reveals that the warmest water masses (ACW and BSW) downwelled from the shelf provide heat over the depth range of 30–70 m in the Canada Basin, while the NVWW and RWW events ventilate the depth range of 70–170 m, encompassing much of the temperature minimum. The inset panel shows that all of the NVWW events and five of the RWW events provide anomalously cold water to the central basin. Thus, the seasonality of the downwelling plays an important role in whether this process warms or cools the interior Beaufort Gyre.

We find that 24 of the 55 events (44%) ventilated the upper halocline (at some period during the event), while only 2 events (4%) ventilated the lower halocline. The latter events immediately followed strong upwelling periods (Lin et al., 2019). In these instances, Atlantic water was upwelled onto the shelf and then immediately fluxed back offshore as a result of downwelling. It is worth noting that there was a 10-day period in April 2003 when the shelfbreak jet advected cold and salty NVWW that was dense enough to ventilate the lower halocline (Spall et al., 2008). However, there were no downwelling events during this period, so the water was not transported offshore. Our results suggest that shelfbreak downwelling in the winter regularly ventilates the upper halocline but only reaches the lower halocline under special circumstances.

Along with tabulating the water masses being downwelled, we also compute the cross-stream volume fluxes. This is done by vertically averaging the cross-stream velocities over the same depth interval at BS3 (50–110 m) and then applying this over the segment of the Beaufort slope corresponding to the average length scale of storms in this region (~500 km; Pickart et al., 2011; Schulze & Pickart, 2012). This yields cross-

a. Westerly storm track (n=24)
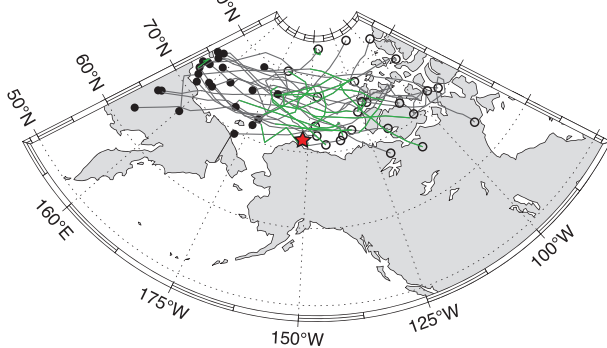
b. Northerly storm track (n=15)
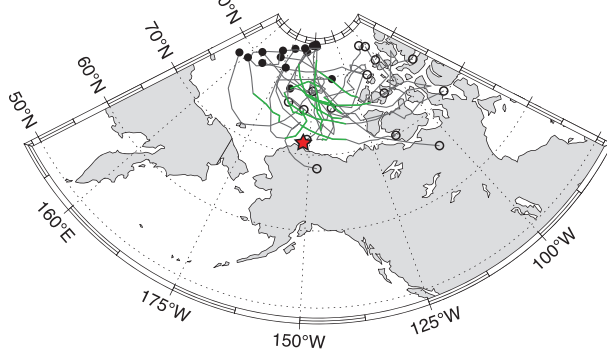
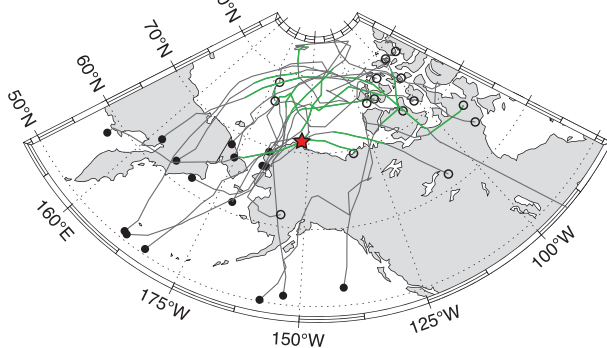**c.** Southerly storm track (n=16)

Figure 14. Tracks of the three groups of storms. (a) Westerly storms that move zonally from northern Siberia and the East Siberian Sea. (b) Northerly storms that originate north of 75°N. (c) Southerly storms that emanate from the North Pacific. In all panels, the solid black circle is the origin of the low-pressure system, the open black circle is the end of the low-pressure system, and the green portion shows the 24-hr period of the storm associated with the maximum along-stream velocity at the shelfbreak. The composites in Figure 15 are averaged over the green portions of the storm tracks. Red stars mark the location of the mooring array.

shelf fluxes of 1.02 ± 0.17 Sv for ACW, 1.10 ± 0.41 Sv for BSW, 0.66 ± 0.27 Sv for RWW, and 0.64 ± 0.25 Sv for NVWW. The volume fluxes of the two summer water masses (ACW and BSW) are statistically different ($p < 0.1$) than the volume fluxes of the winter water masses (RWW and NVWW), but the intraseasonal differences (between ACW and BSW and between RWW and NVWW) are not significant. The seasonality of the storms likely drives this variability, as the colder water masses are commonly fluxed offshore during full and fast ice conditions when the secondary circulation tends to be weaker.

4. Large-Scale Atmospheric Forcing

We now investigate the atmospheric forcing that drives the downwelling along the Alaskan Beaufort slope, using the ERA-I reanalysis fields (see section 2.2). All 55 events were associated with a low-pressure system located offshore of the array. One downwelling event in January 2004 was also accompanied by a strong high-pressure system over the Alaskan North Slope, which likely contributed to the westerly winds, so the ultimate forcing of that single downwelling event was ambiguous. This storm is included in our analysis because the low-pressure system offshore of the mooring array affected the downwelling-favorable winds.

4.1. Storm Tracks and General Characteristics

To track the storms and assess the general characteristics of the downwelling forcing, we identify the low-pressure system responsible for each downwelling event and document its path and evolution through time. The tracking was done manually using the 6-hourly ERA-I fields, since automated routines can have difficulties in cases when storms merge or split. The storm tracking yields three distinct pathways for low-pressure systems to reach the southern Beaufort Sea (Figure 14): a westerly storm track originating in northern Siberia and the East Siberian Sea; a northerly storm track originating from the region north of 75°N; and a southerly storm track stemming from a large area encompassing the Sea of Okhotsk to the Gulf of Alaska. The spread of tracks for the northerly and westerly storms is relatively small, while the southerly storms have a relatively wide geographical spread.

To compare the large-scale atmospheric conditions during these three regimes, we first determine the period of peak downwelling (when the strongest along-stream velocity at the BS3 mooring occurred for each storm) and then average the SLP and 10 m winds over the 24-hr period surrounding this period (green portions of the tracks in Figure 14). We then calculate SLP and wind anomalies from the monthly climatology and average those over the same peak downwelling period (Figure 15, right column). Consider first the westerly storm track case (Figure 15, top row), which accounted for 44% of the storms (24/55). The pattern of SLP and winds is almost exactly opposite of the long-term mean (Figure 2b), with low pressure covering the Beaufort Sea and high pressure in the Bering Sea, resulting in strong westerly winds over the array site. This pattern is mirrored in the SLP anomaly map because the westerly storm tracks are most common in the summer months, when the Aleutian Low and Beaufort High are weakest climatologically (Figure 16). This is likely why there is no signature of the Aleutian Low in the SLP composite.

In the northerly storm track case (Figure 15, middle row), which accounts for 27% (15/55) of the storms, the SLP and winds are quite different. In contrast to the strong meridional dipole of the previous case, there is
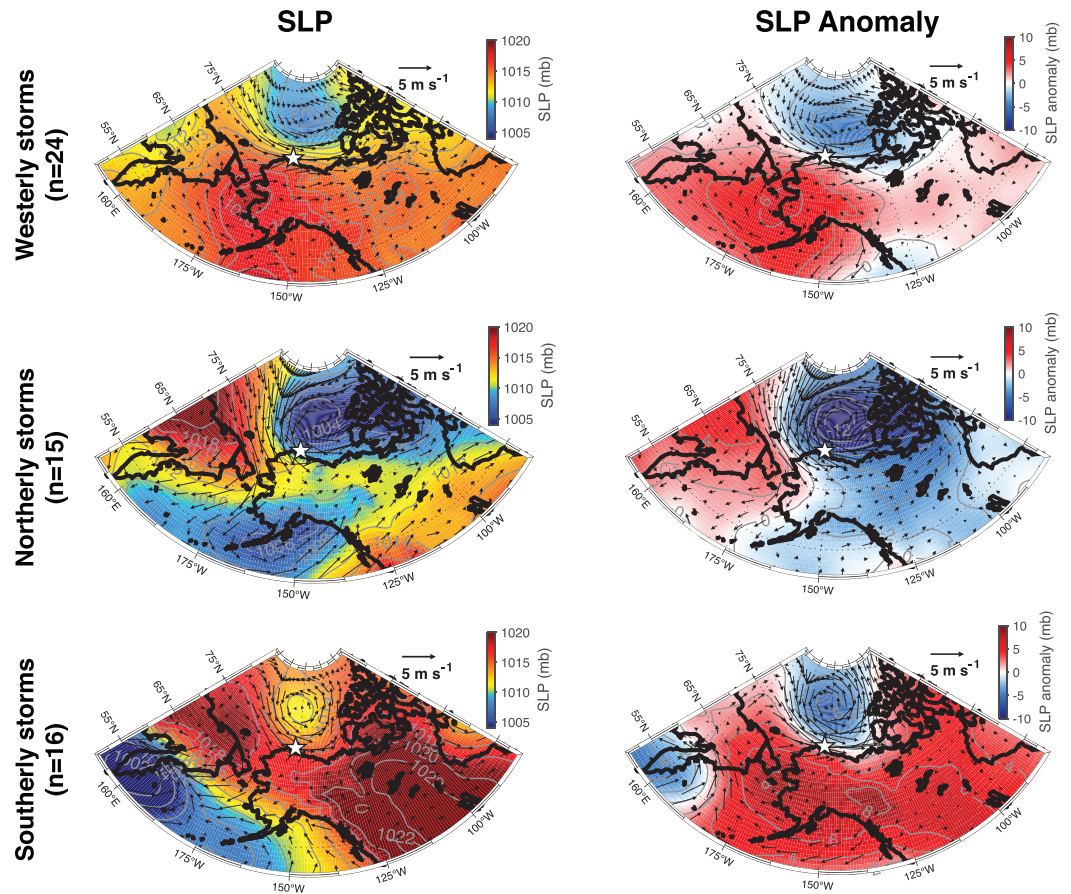
Figure 15. Composites of sea level pressure (colors and gray contours) and 10 m winds (vectors) for the 24-hr period of each storm when the peak along-stream velocity was measured at the shelfbreak (green segments in Figure 14). (left column) The SLP and wind fields for each composite and (right column) the anomalies from the monthly climatology over the same periods. (top row) The composites for the westerly storm track events, (middle row) the composites for the northerly storm track events, and (bottom row) the composites for the southerly storm track events. White stars mark the location of the mooring array.

now a strong zonal dipole associated with the low pressure in the Beaufort Sea and high pressure over Siberia. This drives strong northerly winds in the East Siberian/Chukchi Seas that turn westerly over the southern Beaufort Sea. The minimum low pressure over the Beaufort Sea is lowest in this composite (1,003 mb), and the SLP anomaly is over 12 mb lower than the climatology. Note also that the Aleutian Low is well established in the eastern Bering Sea, and anomalous low pressure covers most of Alaska during these storms.

In the southerly storm track case (Figure 15, bottom row), comprising 29% (16/55) of the storms, the SLP of the composite low is more locally confined than that in the other composites and also less deep (minimum = 1,011 mb). This could be due in part to the wide range of storm tracks comprising this regime (Figure 14c) but is likely also the result of the climatological conditions when this storm track is most active (November, December, and January). These southerly winter storms are acting on a background SLP gradient of a strong Aleutian Low and strengthening Beaufort High (the latter peaks in March/April; Figure 16) that opposes their formation. The anomalies demonstrate that anomalous low pressure covers the Beaufort Gyre and anomalous high pressure resides over Alaska during peak downwelling, resembling a strengthened version of the westerly storm anomaly structure.

4.2. Vertical Structure of Storms

There was an expectation that the northerly, and, to a lesser degree, westerly storms would be mainly barotropic, slow-moving Arctic cyclones, while the storms originating in the low latitudes would be fast-
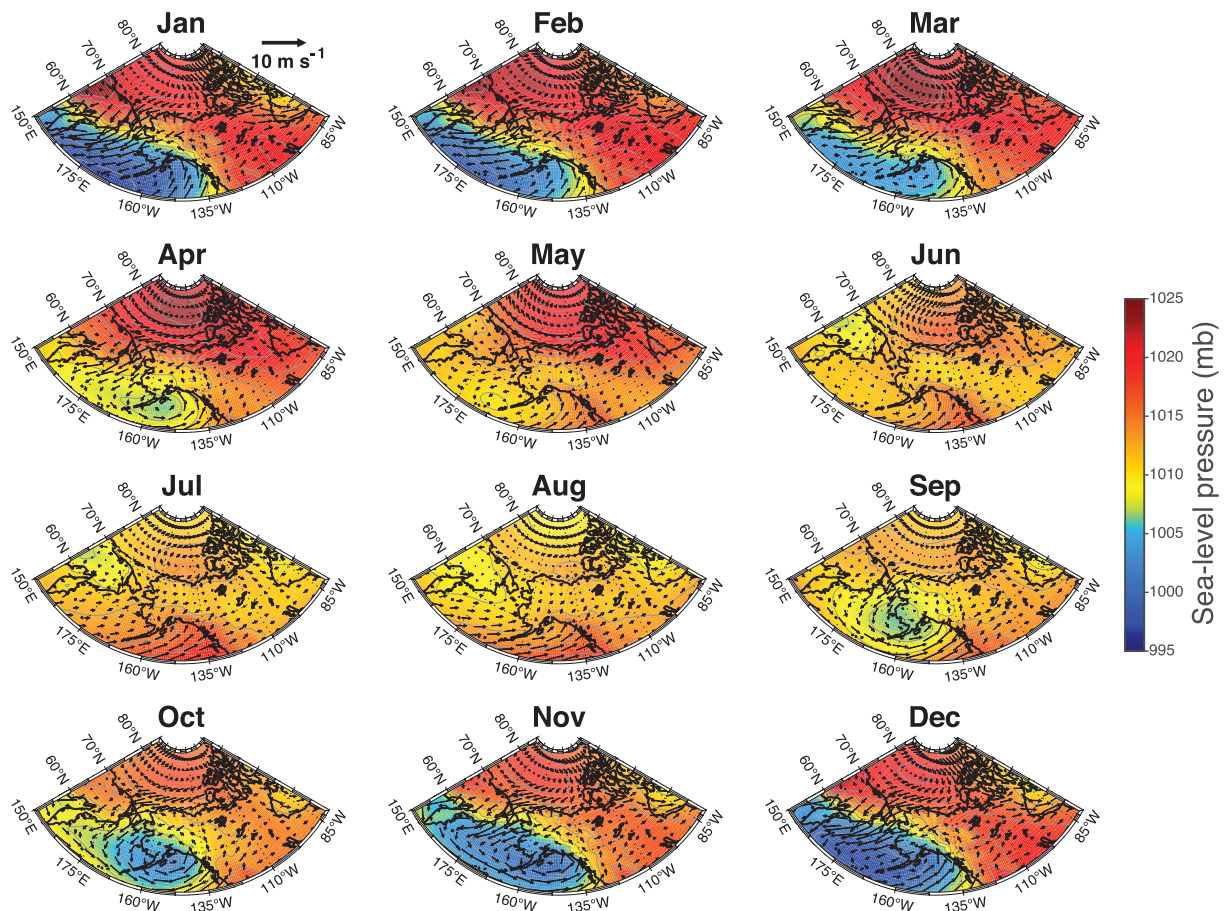
Figure 16. Monthly climatology of SLP and 10-m winds constructed with 37 years of ERA-I data from 1979 to 2015.

moving baroclinic systems (Serreze & Barrett, 2008; Zhang et al., 2004). Baroclinic storms tend to translate more quickly than do barotropic storms because the baroclinicity allows upper-level winds to be stronger. Barotropic storms, on the other hand, draw their energy from coupling to upper-level potential vorticity (PV) anomalies and thus move more slowly (Simmonds & Rudeva, 2012; Tanaka et al., 2012). To test this hypothesis, we compare the storm tracks (based on SLP) to the vertical wind shear for each storm. We find that the storms congregate into three classifications based on their vertical wind shear: baroclinic (large shear), barotropic (weak shear), and instances with a transition from baroclinic to barotropic. Figure 17 provides examples of each of these storm types as their wind shear evolves through time. The westerly storms are nearly split between barotropic (13/24) and baroclinic (9/24) storms, while the northerly storms are primarily barotropic (10/15), consistent with our expectations. The baroclinic-to-barotropic storms encompass the majority (10/16) of the southerly storms. This storm type was not anticipated: these storms originate in the Bering Sea as baroclinic systems and then develop into large, barotropic storms once they come in contact with colder Arctic waters.

There are clear differences regarding the amount of time that the different storm types drive downwelling at the location of the array. The baroclinic-to-barotropic southerly storms tend to stall as they enter the Beaufort Sea, resulting in downwelling at the study site for the longest duration, 4.3 ± 2.1 days. The barotropic northerly storms, which we hypothesized would be the longest-lasting, drive downwelling for 3.8 ± 1.7 days. Following this, the barotropic westerly storms last 3.3 ± 2.0 days. Finally, the baroclinic westerly storms propagate quickly through the region, impacting the study site for only 2.0 ± 1.4 days. Thus, regardless of storm origin or evolution, the barotropic storms linger the longest along the Beaufort slope.
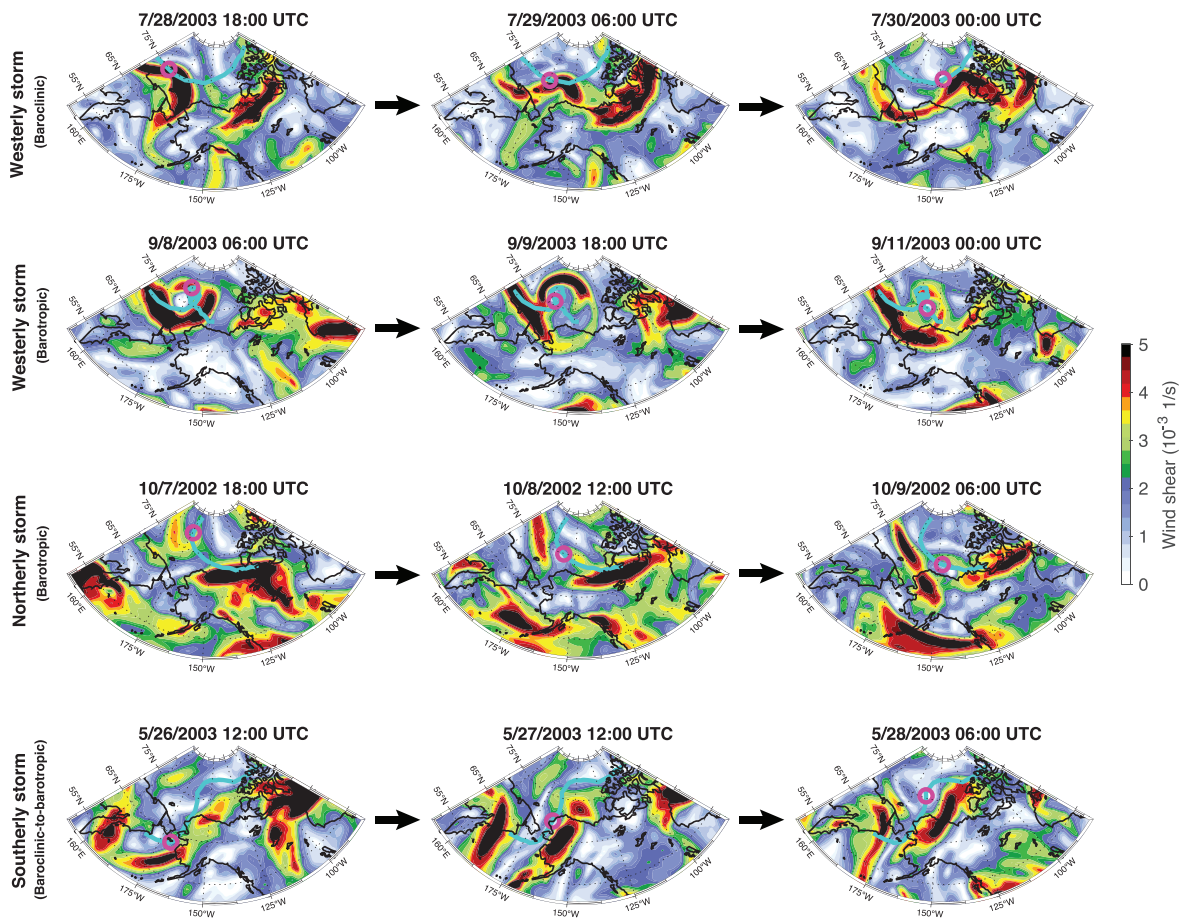
Figure 17. Vertical wind shear during the development of four example storms (see text). (top row) A strong, baroclinic westerly storm in late July 2003. The vertical wind shear (color) is overlain by the storm track (cyan line) and the center of the storm (magenta circle) at the time shown. (second row) A barotropic westerly storm in September 2003 that executes a loop on its path to the Beaufort Sea. (third row) A strong, barotropic northerly storm in October 2002 that descends from near the North Pole. (bottom row) A baroclinic-to-barotropic southerly storm in May 2003 that starts south of Bering Strait in a baroclinic state and then develops into a barotropic cyclone upon entering the Chukchi and Beaufort Seas.

4.3. Seasonality

We now address the seasonality of the storms and their relationship to the ice seasons. Figure 18a shows the monthly distribution of all downwelling storms as both number of events per month (over the 25-month period) and as a percentage of each month. The latter accounts for varying storm durations. The two metrics are consistent, revealing that most downwelling occurs in July and August and that there are relatively few events in February–June. This aligns with the SLP climatology (Figure 16), in which the mean upwelling-favorable SLP structure is strongest in the winter and weakens in July and August.

We present the seasonality of the three storm track regimes in Figure 18b. The westerly storms account for almost the entire peak in July and August, while no westerly events occur in October, December, January, or February. In terms of ice cover, 12 of 24 westerly events occur in open water, while only 3 of 24 occur during fast ice cover. Considering this result in light of the storm track regime composites during peak downwelling (Figure 15), it is seen that the westerly route is most active when there is a strong meridional SLP gradient between high pressure over the eastern Bering Sea and low pressure over the Canada Basin. These conditions likely require strong ocean-to-atmosphere heat fluxes to sustain the anomalous low pressure over the Canada Basin, and open water conditions allow these air-sea fluxes to occur more readily.

In contrast to the westerly storms, none of the southerly storms occur in open water conditions and 10 of the 16 events occur during full ice cover. Though this occurrence of the southerly storms in the winter months seems highly anomalous given the typical Aleutian Low and Beaufort High in these months, the peak in the
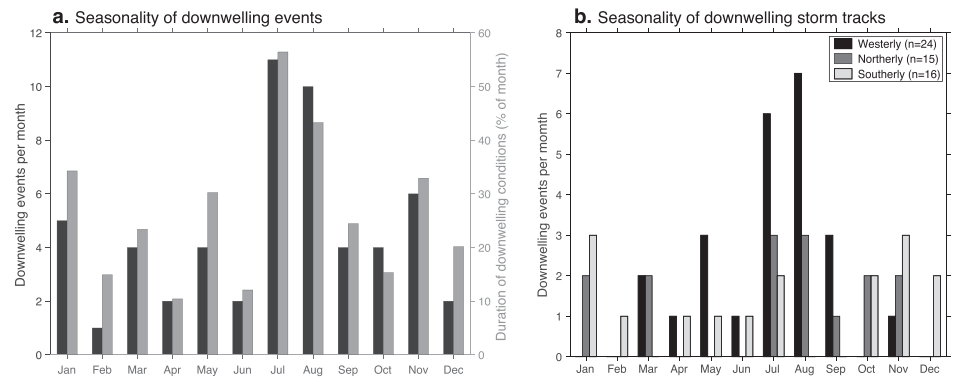
Figure 18. Seasonality of downwelling storms. (a) Frequency of downwelling events per month (black, left y-axis) and duration of downwelling events as a percentage of the month (gray, right y-axis). (b) Monthly climatology of the three storm track regimes.

southerly storms in October–January actually coincides with a period in the SLP climatology (Figure 16) when the Aleutian Low is reaching its strongest (peak in January), but the Beaufort High has still not reached its maximum (peak in March). Thus, the source region (Aleutian Low) for the southerly storms is strong, while the inhibiting factor (Beaufort High) has not yet fully strengthened. The seasonality of northerly storms is less clear (7/15 in open water, 2/15 in partial ice, 3/15 in full ice, and 3/15 in fast ice), though it is most similar to the seasonality of the westerly storms. On the whole, the seasonality of the downwelling events aligns closely with what we would expect from the SLP climatology.

5. Conclusions and Discussion

We characterize the oceanographic response and atmospheric forcing associated with downwelling along the Alaskan Beaufort shelf/slope, using data from an array of eight moorings situated 150 km to the east of Pt. Barrow. During the two-year study period (August 2002 to September 2004) we find that downwelling is ubiquitous: There are 55 events in total, with at least one event occurring in 24 of the 25 months. A series of eight consecutive downwelling storms in July 2003 covered three-quarters of the month, while no events occurred in April 2004. Canonical downwelling occurs most often in July and August during ice retreat and open water conditions, as the SLP gradient between the Aleutian Low and Beaufort High relaxes in the summer months. The typical sequence of events is as follows. Large, cyclonic storms arrive in the southern Canada Basin and displace the Beaufort High. The along-coast winds reverse from the typical upwelling-favorable easterly direction to westerly. About 8-hr later, the eastward flowing shelfbreak jet accelerates, followed roughly 4-hr later by a depression of isopycnals along the outer-shelf and slope. The typical downwelling storm lasts a little over 3 days, at which point the winds relax and return to their easterly state before the oceanographic response concludes. The shelfbreak jet slows to its typical state, and, finally, the isopycnals rebound. We do not see evidence of a "rebound jet" as was documented in Pickart et al. (2011) following upwelling events.

We characterize the forcing of each storm by the cumulative Ekman transport and use the time integral of the near-bottom density anomaly in the vicinity of the shelfbreak as a measure of the downwelling response. Based on these metrics, the strength of the oceanographic response is strongly connected to the strength of the wind forcing in a manner analogous to upwelling. Also similar to upwelling, the downwelling response is greatest during partial ice conditions, followed by comparable signals for open water and full (but mobile) ice cover. The weakest response occurs in the fast ice season. These trends are understandable in terms of the impact of ice cover on the surface stress. For freely moving ice keels (partial ice) the ice-ocean stress enhances the overall response (e.g., Pickart, Spall, & Mathis, 2013), while the transfer of wind stress to the ocean is inhibited by internal ice stress for full ice conditions. Subdued responses during periods of fast ice are likely due to nonlocal forcing in adjacent regions of open water or lighter ice cover (which was found to be the case for upwelling; Schulze & Pickart, 2012). One caveat here is that wind speeds are generally stronger during the open water season. Consequently, the shelfbreak jet intensifies the most then, and the cross-stream Ekman flow is also largest during this season.

The impact of the downwelling events on the shelf-basin exchange of water varies considerably across seasons. In ice-free conditions (July, August, and September), the warm and relatively fresh ACW and BSW are typically present at depth near the shelfbreak and are thus transported offshore. These water masses provide heat and freshwater to the upper layers of the Canada Basin and strengthen the density contrast between the light Pacific waters and underlying dense Atlantic waters. In the winter months, Pacific winter waters—both newly ventilated and remnant—occupy the shelf. When these are downwelled they ventilate the upper halocline of the Canada Basin. The offshore fluxes of these various water masses are considerable: >1 Sv for the summer water masses and ~0.6–0.7 Sv for the winter water masses. As such, they represent a significant pathway for shelf-basin exchange and the spreading of Pacific-origin waters into the interior Arctic, albeit intermittently.

In each of the 55 downwelling events, a low-pressure system was situated offshore of the mooring array. Manual storm tracking reveals that there were three main routes by which the storms ended up at this location. Most of the storms originate from the west in the vicinity of the East Siberian Sea, followed by roughly an equal number emanating from the high Arctic and from south of Bering Strait. There are differences as well in the vertical structure of the storms. Barotropic storms tend to be of Arctic origin, arriving along the westerly or northerly routes, while baroclinic storms arrive from the west. The baroclinic-to-barotropic storms typically follow the southerly route through Bering Strait and across the Chukchi Sea. The wind shear is strongly linked to the duration of downwelling at the array site, as baroclinic storms move rapidly through the region, while the barotropic storms are more slow-moving.

It is important to note that the seasonal cycle reported here is based on only 2 years of data; thus, our results may not be representative of other years. Anomalies from the seasonal SLP climatology (not shown) indicate that the SLP across the Beaufort Sea in July 2003 was 2–3 standard deviations lower than the mean July conditions. Moore (2012) reconstruct summer variability in the Beaufort High from 1948 to 2011, and 2002–2003 stand out as two of the three weakest Beaufort Highs in the record. Since 2002, there has been a steady increase in the strength of the summer Beaufort High (Moore, 2012), indicating a potential decrease of summer downwelling storms. This strengthening of the summer Beaufort High is also linked to the lengthening ice-free conditions in the region (Moore, 2012). These two effects oppose one another in determining the number of downwelling storms that occur during ice-free conditions, and it is unclear at this point which effect dominates. The rapid increase in erosion rates at Drew Point (Jones et al., 2018) and along the Alaskan North Slope indicates that there has been an increase in downwelling storms during ice-free conditions, though this has not yet been documented. In the winter months, a collapse of the Beaufort High in the winter of 2017 was driven by anomalous cyclonic storms propagating along the East Siberian Coast and into the Arctic (Moore et al., 2018), possibly leading to downwelling at the study site. Thus, the occurrence of winter downwelling-favorable storms may be increasing as the winter Beaufort High weakens into the future. Overall, our seasonal cycle of downwelling storms is largely consistent with the seasonality one would expect from the SLP monthly climatology (Figure 16; data from 1979 to 2015). Therefore, we anticipate that our finding of increased downwelling events in July and August is robust, though the degree to which the magnitude of our seasonality matches the long-term seasonality remains an open question.

References

Barnhart, K. R., Overeem, I., & Anderson, R. S. (2014). The effect of changing sea ice on the physical vulnerability of Arctic coasts. *The Cryosphere*, *8*(5), 1777–1799. https://doi.org/10.5194/tc-8-1777-2014

Barnhart, K. R., Anderson, R. S., Overeem, I., Wobus, C., Clow, G. D., & Urban, F. E. (2014). Modeling erosion of ice-rich permafrost bluffs along the Alaskan Beaufort Sea coast. *Journal of Geophysical Research: Earth Surface*, *119*, 1155–1179. https://doi.org/10.1002/2013JF002845

Behrendt, A., Sumata, H., Rabe, B., & Schauer, U. (2018). UDASH—Unified Database for Arctic and Subarctic Hydrography. *Earth System Science Data*, *10*(2), 1119–1138. https://doi.org/10.5194/essd-10-1119-2018

Brugler, E. T., Pickart, R. S., Moore, G. W. K., Roberts, S., Weingartner, T. J., & Statscewich, H. (2014). Seasonal to interannual variability of the Pacific water boundary current in the Beaufort Sea. *Progress in Oceanography*, *127*, 1–20. https://doi.org/10.1016/j.pocean.2014.05.002

Coachman, L. K., Aagaard, K., & Tripp, R. B. (1975). Bering Strait: The regional physical oceanography. ARCTIC. https://doi.org/10.14430/arctic3020

Corlett, W. B., & Pickart, R. S. (2017). The Chukchi slope current. *Progress in Oceanography*, *153*, 50–65. https://doi.org/10.1016/j.pocean.2017.04.005

Cunliffe, A. M., Tanski, G., Radosavljevic, B., Palmer, W. F., Sachs, T., Lantuit, H., et al. (2018). Rapid retreat of permafrost coastline observed with aerial drone photogrammetry. *The Cryosphere Discussions*, 1–27. https://doi.org/10.5194/tc-2018-234

Dee, D. P., Uppala, S. M., Simmons, A. J., Berrisford, P., Poli, P., Kobayashi, S., et al. (2011). The ERA-Interim reanalysis: Configuration and performance of the data assimilation system. *Quarterly Journal of the Royal Meteorological Society*, *137*(656), 553–597. https://doi.org/10.1002/qj.828

Dmitrenko, I. A., Kirillov, S. A., Forest, A., Gratton, Y., Volkov, D. L., Williams, W. J., et al. (2016). Shelfbreak current over the Canadian Beaufort Sea continental slope: Wind-driven events in January 2005. *Journal of Geophysical Research: Oceans*, *121*, 2447–2468. https://doi.org/10.1002/2015JC011514

Dmitrenko, I. A., Kirillov, S. A., Myers, P. G., Forest, A., Tremblay, B., Lukovich, J. V., et al. (2018). Wind-forced depth-dependent currents over the eastern Beaufort Sea continental slope: Implications for Pacific water transport. *Elem Sci Anth*, *6*(1), 66. https://doi.org/10.1525/elementa.321

Fine, E. C., MacKinnon, J. A., Alford, M. H., & Mickett, J. B. (2018). Microstructure observations of turbulent heat fluxes in a warm-core Canada Basin eddy. *Journal of Physical Oceanography*, *48*(10), 2397–2418. https://doi.org/10.1175/jpo-d-18-0028.1

Fratantoni, P. S., Zimmermann, S., Pickart, R. S., & Swartz, M. (2006). Western Arctic Shelf-Basin Interactions Experiment : Processing and calibration of moored profiler data from the Beaufort Shelf Edge mooring array. *Western Arctic Shelf-Basin Interactions Experiment: Processing and Calibration of Moored Profiler Data from the Beaufort Shelf Edge Mooring Array*, (December). https://doi.org/10.1575/1912/1429

Frey, K. E., Moore, G. W. K., Cooper, L. W., & Grebmeier, J. M. (2015). Divergent patterns of recent sea ice cover across the Bering, Chukchi, and Beaufort Seas of the Pacific Arctic Region. *Progress in Oceanography*, *136*, 32–49. https://doi.org/10.1016/j.pocean.2015.05.009

Gong, D., & Pickart, R. S. (2016). Early summer water mass transformation in the eastern Chukchi Sea. *Deep-Sea Research Part II: Topical Studies in Oceanography*, *130*, 43–55. https://doi.org/10.1016/j.dsr2.2016.04.015

Huyer, A., Sobey, E., & Smith, R. L. (1979). The spring transition in currents over the Oregon continental shelf. *Journal of Geophysical Research*, *84*, 6995–7011.

Jones, B. M., Arp, C. D., Jorgenson, M. T., Hinkel, K. M., Schmutz, J. A., & Flint, P. L. (2009). Increase in the rate and uniformity of coastline erosion in Arctic Alaska. *Geophysical Research Letters*, *36*, L03503. https://doi.org/10.1029/2008GL036205

Jones, B. M., Farquharson, L. M., Baughman, C. A., Buzard, R. M., Arp, C. D., Grosse, G., et al. (2018). A decade of remotely sensed observations highlight complex processes linked to coastal permafrost bluff erosion in the Arctic. *Environmental Research Letters*, *13*(11). https://doi.org/10.1088/1748-9326/aae471

Kirillov, S., Dmitrenko, I., Tremblay, B., Gratton, Y., Barber, D., & Rysgaard, S. (2016). Upwelling of Atlantic water along the Canadian Beaufort Sea continental slope: Favorable atmospheric conditions and seasonal and interannual variations. *Journal of Climate*, *29*, 4509–4523. https://doi.org/10.1175/JCLI-D-15-0804.1

Krishfield, R., Toole, J., Proshutinsky, A., & Timmermans, M. L. (2008). Automated ice-tethered profilers for seawater observations under pack ice in all seasons. *Journal of Atmospheric and Oceanic Technology*, *25*(11), 2091–2105. https://doi.org/10.1175/2008JTECHO587.1

Li, M., Pickart, R. S., Spall, M. A., Weingartner, T. J., Lin, P., Moore, G. W. K., & Qi, Y. (2019). Circulation of the Chukchi Sea shelfbreak and slope from moored timeseries. *Progress in Oceanography*, *172*, 14–33. https://doi.org/10.1016/j.pocean.2019.01.002

Lin, P., Pickart, R. S., Moore, G. W. K., Spall, M. A., & Hu, J. (2019). Characteristics and dynamics of wind-driven upwelling in the Alaskan Beaufort Sea based on six years of mooring data. *Deep-Sea Research Part II: Topical Studies in Oceanography*, *162*, 79–92. https://doi.org/10.1016/j.dsr2.2018.01.002

Lin, P., Pickart, R. S., Stafford, K. M., Moore, G. W. K., Torres, D. J., Bahr, F., & Hu, J. (2016). Seasonal variation of the Beaufort shelfbreak jet and its relationship to Arctic cetacean occurrence. *Journal of Geophysical Research: Oceans*, *121*, 8434–8454. https://doi.org/10.1002/2016JC022890

Linders, J., Pickart, R. S., Björk, G., & Moore, G. W. K. (2017). On the nature and origin of water masses in Herald Canyon, Chukchi Sea: Synoptic surveys in summer 2004, 2008, and 2009. *Progress in Oceanography*, *159*, 99–114. https://doi.org/10.1016/j.pocean.2017.09.005

Manley, T. O., & Hunkins, K. (1985). Mesoscale eddies of the Arctic Ocean. *Journal of Geophysical Research*, *90*(C3), 4911. https://doi.org/10.1029/jc090ic03p04911

Martin, T., Steele, M., & Zhang, J. (2014). Seasonality and long-term trend of Arctic Ocean surface stress in a model. *Journal of Geophysical Research: Oceans*, *119*, 1723–1738. https://doi.org/10.1002/2013JC009425

Mathis, J. T., Pickart, R. S., Hansell, D. A., Kadko, D., & Bates, N. R. (2007). Eddy transport of organic carbon and nutrients from the Chukchi Shelf: Impact on the upper halocline of the western Arctic Ocean. *Journal of Geophysical Research*, *112*, C05011. https://doi.org/10.1029/2006JC003899

Moore, G. W. K. (2012). Decadal variability and a recent amplification of the summer Beaufort Sea High. *Geophysical Research Letters*, *39*, L10807. https://doi.org/10.1029/2012GL051570

Moore, G. W. K., Schweiger, A., Zhang, J., & Steele, M. (2018). Collapse of the 2017 winter Beaufort High: A response to thinning sea ice? *Geophysical Research Letters*, *45*, 2860–2869. https://doi.org/10.1002/2017GL076446

Nikolopoulos, A., Pickart, R. S., Fratantoni, P. S., Shimada, K., Torres, D. J., & Jones, E. P. (2009). The western Arctic boundary current at 152°W: Structure, variability, and transport. *Deep-Sea Research Part II: Topical Studies in Oceanography*, *56*(17), 1164–1181. https://doi.org/10.1016/j.dsr2.2008.10.014

Perovich, D. (2011). The changing Arctic sea ice cover. *Oceanography*, *24*(3), 162–173. https://doi.org/10.5670/oceanog.2011.68

Pickart, R. S. (2004). Shelfbreak circulation in the Alaskan Beaufort Sea: Mean structure and variability. *Journal of Geophysical Research*, *109*, C04024. https://doi.org/10.1029/2003JC001912

Pickart, R. S., Moore, G. W. K., Torres, D. J., Fratantoni, P. S., Goldsmith, R. A., & Yang, J. (2009). Upwelling on the continental slope of the Alaskan Beaufort Sea: Storms, ice, and oceanographic response. *Journal of Geophysical Research*, *114*, C00A13. https://doi.org/10.1029/2008JC005009

Pickart, R. S., Nobre, C., Lin, P., Arrigo, K. R., Ashjian, C. J., Berchok, C., et al. (2019). Seasonal to mesoscale variability of water masses and atmospheric conditions in Barrow Canyon, Chukchi Sea. *Deep-Sea Research Part II: Topical Studies in Oceanography*, *162*, 32–49. https://doi.org/10.1016/j.dsr2.2019.02.003

Pickart, R. S., Pratt, L. J., Torres, D. J., Whitledge, T. E., Proshutinsky, A. Y., Aagaard, K., et al. (2010). Evolution and dynamics of the flow through Herald Canyon in the western Chukchi Sea. *Deep-Sea Research Part II: Topical Studies in Oceanography*, *57*(1-2), 5–26. https://doi.org/10.1016/j.dsr2.2009.08.002

Pickart, R. S., Schulze, L. M., Moore, G. W. K., Charette, M. A., Arrigo, K. R., van Dijken, G., & Danielson, S. L. (2013). Long-term trends of upwelling and impacts on primary productivity in the Alaskan Beaufort Sea. *Deep-Sea Research Part I: Oceanographic Research Papers*, *79*, 106–121. https://doi.org/10.1016/j.dsr.2013.05.003

Pickart, R. S., Spall, M. A., & Mathis, J. T. (2013). Dynamics of upwelling in the Alaskan Beaufort Sea and associated shelf-basin fluxes. *Deep-Sea Research Part I: Oceanographic Research Papers*, *76*, 35–51. https://doi.org/10.1016/j.dsr.2013.01.007

Pickart, R. S., Spall, M. A., Moore, G. W. K., Weingartner, T. J., Woodgate, R. A., Aagaard, K., & Shimada, K. (2011). Upwelling in the Alaskan Beaufort Sea: Atmospheric forcing and local versus non-local response. *Progress in Oceanography*, *88*(1–4), 78–100. https://doi.org/10.1016/j.pocean.2010.11.005

Pickart, R. S., & Stossmeister, G. (2008). Outflow of Pacific water from the Chukchi Sea to the Arctic Ocean. *Chinese Journal of Polar Oceanography*, *19*(2), 135–148.

Pickart, R. S., Weingartner, T. J., Pratt, L. J., Zimmermann, S., & Torres, D. J. (2005). Flow of winter-transformed Pacific water into the Western Arctic. *Deep-Sea Research Part II: Topical Studies in Oceanography.*, *52*(24-26), 3175–3198. https://doi.org/10.1016/j.dsr2.2005.10.009

Pisareva, M., Pickart, R., Iken, K., Ershova, E., Grebmeier, J., Cooper, L., et al. (2015). The relationship between patterns of benthic fauna and zooplankton in the Chukchi Sea and physical forcing. *Oceanography*, *28*(3), 68–83. https://doi.org/10.5670/oceanog.2015.58

Pite, H. D., Topham, D. R., & van Hardenberg, B. J. (2002). Laboratory measurements of the drag force on a family of two-dimensional ice keel models in a two-layer flow. *Journal of Physical Oceanography*, *25*(12), 3008–3031. https://doi.org/10.1175/1520-0485(1995)025<3008:lmotdf>2.0.co;2

Proshutinsky, A., Dukhovskoy, D., Timmermans, M. L., Krishfield, R., & Bamber, J. L. (2015). Arctic circulation regimes. *Philosophical Transactions of the Royal Society A: Mathematical, Physical and Engineering Sciences*, *373*(2052). https://doi.org/10.1098/rsta.2014.0160

Schulze, L. M., & Pickart, R. S. (2012). Seasonal variation of upwelling in the Alaskan Beaufort Sea: Impact of sea ice cover. *Journal of Geophysical Research*, *117*, C06022. https://doi.org/10.1029/2012JC007985

Serreze, M. C., & Barrett, A. P. (2008). The summer cyclone maximum over the central Arctic Ocean. *Journal of Climate*, *21*(5), 1048–1065. https://doi.org/10.1175/2007JCLI1810.1

Simmonds, I., & Rudeva, I. (2012). The great Arctic cyclone of August 2012. *Geophysical Research Letters*, *39*, L23709. https://doi.org/10.1029/2012GL054259

Spall, M. A., Pickart, R. S., Fratantoni, P. S., & Plueddemann, A. J. (2008). Western Arctic shelfbreak eddies: Formation and transport. *Journal of Physical Oceanography*, *38*(8), 1644–1668. https://doi.org/10.1175/2007jpo3829.1

Spall, M. A., Pickart, R. S., Li, M., Itoh, M., Lin, P., Kikuchi, T., & Qi, Y. (2018). Transport of Pacific water into the Canada Basin and the formation of the Chukchi Slope Current. *Journal of Geophysical Research: Oceans*, *123*, 7453–7471. https://doi.org/10.1029/2018JC013825

Spreen, G., Kaleschke, L., & Heygster, G. (2008). Sea ice remote sensing using AMSR-E 89 GHz channels. *Journal of Geophysical Research*, *113*, C02S03. https://doi.org/10.1029/2005JC003384

Steele, M., Morison, J., Ermold, W., Rigor, I., Ortmeyer, M., & Shimada, K. (2004). Circulation of summerPacific halocline water in the Arctic Ocean. *Journal of Geophysical Research*, *109*, C02027. https://doi.org/10.1029/2003JC002009

Tanaka, H. L., Yamagami, A., & Takahashi, S. (2012). The structure and behavior of the arctic cyclone in summer analyzed by the JRA-25/JCDAS data. *Polar Science*, *6*(1), 55–69. https://doi.org/10.1016/j.polar.2012.03.001

Timmermans, M. L., Marshall, J., Proshutinsky, A., & Scott, J. (2017). Seasonally derived components of the Canada Basin halocline. *Geophysical Research Letters*, *44*, 5008–5015. https://doi.org/10.1002/2017GL073042

Toole, J., Krishfield, R., Timmermans, M.-L., & Proshutinsky, A. (2011). The ice-tethered profiler: Argo of the Arctic. *Oceanography*, *24*(3), 126–135. https://doi.org/10.5670/oceanog.2011.64

von Appen, W.-J., & Pickart, R. S. (2011). Two configurations of the Western Arctic Shelfbreak Current in summer. *Journal of Physical Oceanography*, *42*(3), 329–351. https://doi.org/10.1175/jpo-d-11-026.1

von Appen, W., & Pickart, R. S. (2012). Two configurations of the western Arctic shelfbreak current in summer. *Journal of Physical Oceanography*, *78*(1), 58–77.

Watanabe, E. (2011). Beaufort shelf break eddies and shelf-basin exchange of Pacific summer water in the western Arctic Ocean detected by satellite and modeling analyses. *Journal of Geophysical Research*, *116*, C08034. https://doi.org/10.1029/2010JC006259

Williams, W. J., Carmack, E. C., Shimada, K., Melling, H., Aagaard, K., Macdonald, R. W., & Grant Ingram, R. (2006). Joint effects of wind and ice motion in forcing upwelling in Mackenzie Trough, Beaufort Sea. *Continental Shelf Research*, *26*(19), 2352–2366. https://doi.org/10.1016/j.csr.2006.06.012

Woodgate, R. A. (2018). Increases in the Pacific inflow to the Arctic from 1990 to 2015, and insights into seasonal trends and driving mechanisms from year-round Bering Strait mooring data. *Progress in Oceanography*, *160*, 124–154. https://doi.org/10.1016/j.pocean.2017.12.007

Woodgate, R. A., & Aagaard, K. (2005). Revising the Bering Strait freshwater flux into the Arctic Ocean. *Geophysical Research Letters*, *32*, L02602. https://doi.org/10.1029/2004GL021747

Zhang, X., Walsh, J. E., Zhang, J., Bhatt, U. S., & Ikeda, M. (2004). Climatology and interannual variability of Arctic cyclone activity: 1948–2002. *Journal of Climate*, *17*(12), 2300–2317. https://doi.org/10.1175/1520-0442(2004)017<2300:CAIVOA>2.0.CO;2

Zhao, M., & Timmermans, M. L. (2015). Vertical scales and dynamics of eddies in the Arctic Ocean's Canada Basin. *Journal of Geophysical Research: Oceans*, *120*, 8195–8209. https://doi.org/10.1002/2015JC011251